HHS Public Access

Author manuscript

Cell Rep. Author manuscript; available in PMC 2025 April 07.

Published in final edited form as:

Cell Rep. 2025 March 25; 44(3): 115377. doi:10.1016/j.celrep.2025.115377.

Mitochondrial fusion and cristae reorganization facilitate acquisition of cardiomyocyte identity during reprogramming of murine fibroblasts

Brian M. Spurlock[1,4], **Yifang Xie**[1,4], **Yiran Song**[1], **Shea N. Ricketts**[1,2], **James Rock Hua**[1], **Haley R. Chi**[1,2], **Meenakshi Nishtala**[1], **Rustem Salmenov**[1], **Jiandong Liu**[1], **Li Qian**[1,3,5,*]

[1]McAllister Heart Institute, University of North Carolina, Chapel Hill, NC 27599, USA

[2]Department of Pathology and Laboratory Medicine, University of North Carolina, Chapel Hill, NC 27599, USA

[3]Present address: 111 Mason Farm Rd., Chapel Hill, NC 27599, USA

[4]These authors contributed equally

[5]Lead contact

SUMMARY

Cardiomyocytes (CMs) rely on mitochondrial energy produced in highly interconnected mitochondrial networks. Direct reprogramming of cardiac fibroblasts (CFs) into induced CMs (iCMs) shows promise for treating cardiac injury, but little work has investigated mitochondrial energetics and morphology during the conversion of CFs to iCMs. We characterized mitochondria during direct cardiac reprogramming of murine neonatal CFs (mnCFs). Reprogramming increased mitochondrial respiration and interconnectivity but not to the levels of native CMs. We therefore investigated whether perturbations to mitochondrial dynamics impacted reprogramming. Mitochondrial fusion (joining) was essential for iCM generation, while various fission (dividing) genes were reprogramming barriers. In particular, the loss of mitochondrial fission regulator 1 like (*Mtfr1l*) significantly increased the yield of functionally mature iCMs and induced mitochondrial fusion and respiration. These changes were countered by the concomitant loss of fusion effector optical atrophy protein 1 (*Opa1*). The present study advances our understanding of mitochondrial barriers to and mechanisms of direct cardiac reprogramming.

Graphical abstract

*Correspondence: li_qian@med.unc.edu.

AUTHOR CONTRIBUTIONS

Conceptualization, B.M.S., Y.X., H.R.C., J.L., and L.Q.; methodology, B.M.S., Y.X., Y.S., J.R.H., R.S., and M.N.; investigation, B.M.S., Y.X., Y.S., S.R., J.R.H., R.S., and M.N.; visualization, B.M.S., Y.X., and S.R.; supervision, J.L. and L.Q.; writing – original draft, B.M.S., Y.X., and J.R.H.; writing – review & editing, B.M.S., Y.X., S.R., J.L., and L.Q.

DECLARATION OF INTERESTS

The authors declare that they have no competing interests.

SUPPLEMENTAL INFORMATION

Supplemental information can be found online at https://doi.org/10.1016/j.celrep.2025.115377.

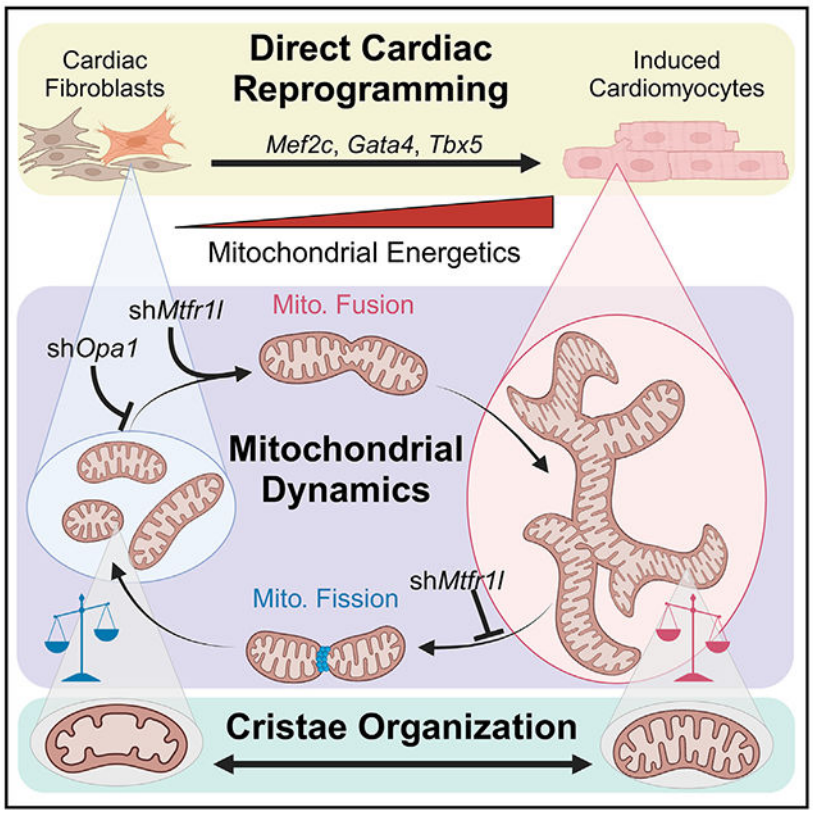

In brief

Spurlock et al. characterize shifts in mitochondrial energetics and morphology during the direct cardiac reprogramming of murine fibroblasts. They show that mitochondrial fusion is required for the acquisition of cardiomyocyte-like identity and identify the fission regulator *Mtfr1l* as a potent barrier to reprogramming.

INTRODUCTION

Differentiation from nascent to mature cardiomyocytes (CMs),[1] or from induced pluripotent stem cells (iPSCs) to CMs,[2] requires metabolic reprogramming from primarily glycolytic to primarily mitochondrial energetics. Reversing this shift is sufficient to induce proliferation in quiescent CMs.[3–5] Together, these data suggest that mitochondrial respiration is key to forming and maintaining mature CMs. Indeed, various factors that promote the reprogramming of non-CMs to functional CMs are known to either inhibit pro-glycolytic pathways[6–8] or promote mitochondrial respiration.[9–11]

Mitochondria generate an electrochemical gradient across their inner membrane (IMM [inner mitochondrial membrane]), which can be harnessed to produce ATP, reactive oxygen species (ROS), or heat.[12] The energetics of mitochondria is influenced by their morphology, largely determined by the dynamic balance of opposing fusion (joining) and fission (dividing) of their outer membranes (OMMs [outer mitochondrial membranes]) and inner membranes. Increased fusion activity leading to larger mitochondrial networks is associated

with higher ATP production.[13,14] In addition, cristae, folds of the IMM that are the major sites of energy production, increase in number and density with increased mitochondrial energetics.[15] Mitochondria in striated muscle segregate into highly fused intrafibrillar mitochondria (IFMs) and peripheral mitochondria. The former facilitate muscle contraction, while the latter shuttle ATP and signaling molecules to neighboring cells or the nucleus.[16,17] IFMs are translocated to nascent myofibrils via sarcoplasmic reticulum (SR) contact sites, some of which are maintained for calcium signaling in mature CMs.[12,16,18]

Ischemic heart disease, including myocardial infarction (MI), remains the leading cause of death worldwide.[19] Because mature mammalian CMs lack proliferative capacity,[20,21] muscle loss during MI is irreversible.[22] The injury is populated with cardiac fibroblasts (CFs) that form less functional scar tissue, which often leads to heart failure. We and others have identified factors that can reprogram CFs into functional induced CMs (iCMs).[23–25] Much work has investigated the genetic,[26] epigenetic,[27] and, more recently, translational[28] mechanisms of cardiac reprogramming. However, little is known about mitochondrial or metabolic barriers to iCM generation.

Compared to CMs, the mitochondria of CFs are fewer, more fragmented (higher fission), less cristae dense, and less energetically active.[29] Successful cardiac reprogramming to a mature phenotype, therefore, requires increased mitochondrial biogenesis, fusion, and respiration in nascent iCMs. In keeping with this, some reprogramming factors promote fusion or inhibit fission alongside their canonical reprogramming roles.[9,10,30] However, the metabolic shift and mitochondrial reorganization underlying iCM conversion remain largely unknown. To address this knowledge gap, we investigate two critical questions: how do mitochondria change during cardiac reprogramming and can inducing CM-like mitochondrial morphology increase the yield of mature iCMs?

We characterized mitochondrial energetics and dynamics during cardiac reprogramming of murine fibroblasts. Over several weeks, reprogramming increased mitochondrial fusion, biogenesis, and respiration, but this mitochondrial reorganization was incomplete relative to native CMs. We then assessed how perturbations to mitochondrial dynamics impact cardiac reprogramming efficiency. The major mitochondrial fusion effectors, optical atrophy protein 1 (*Opa1*) on the IMM and mitofusins 1 and 2 (*Mfn1/2*) on the OMM,[13] were necessary for successful cardiac reprogramming. Importantly, the little-studied mitochondrial fission regulator 1-like protein (*Mtfr1l*)[31] was a potent barrier to the generation of mature iCMs. Finally, we developed a machine learning model to evaluate reprogramming in live cells using mitochondrial metrics. The model's prediction matched the trends of assessments of reprogramming through expression of CM markers.

Mtfr1l is a cytosolic protein associated with the OMM[31] identified by shotgun sequencing.[32,33] Recent studies implicate *Mtfr1l* in regulating iron-sulfur clusters,[34] cuproptosis,[35] and mitochondrial localization to neuron dendrites.[36] Upon phosphorylation by AMPK, MTFR1L facilitates the cleavage of OPA1[31] to its short form (OPA1-s), which does not participate in fusion.[37] This may form part of a nutrient-sensing feedback mechanism regulating mitochondrial structure.[38] MTFR1L also participates in cristae organization through interactions with OPA1 and MIC60.[39] We, therefore, hypothesize

that the loss of *Mtfr1l* increases the yield of mature iCMs by promoting mitochondrial fusion and cristae reorganization leading to enhanced mitochondrial energetics. By studying mitochondrial regulation of CF and CM identity, we advance our understanding of the metabolic mechanisms of cardiac reprogramming and identify *Mtfr1l* as a potent reprogramming barrier.

RESULTS

Quantitative comparison of mitochondrial energetics and structure in mnCFs and CMs

To evaluate mitochondria during reprogramming, we first isolated CFs and CMs from neonatal mice (murine neonatal CFs [mnCFs], ~90% purity, and mnCMs, ~70% purity) (Figures 1A and S1A–S1F). We performed mitochondrial stress tests (MSTs)[40] 48 h after seeding mnCFs and mnCMs to measure mitochondrial oxygen consumption rates (OCRs). Expectedly, mnCMs had significantly higher basal, ATP-linked, ROS-linked (proton leak), and maximal mitochondrial respiration[40] (Figures 1B and 1C). We observed no significant change in the difference between basal and maximal OCRs, called spare respiratory capacity or reserve OCRs. This means that mnCMs and mnCFs share a similar capacity to ramp up mitochondrial energy production in response to stress or other stimuli.

We also quantified mitochondrial structure and function in live single cells using the MitoSinCe2 workflow to analyze high-resolution three-dimensional (3D) images of mitochondria stained with MitoTracker Deep Red (MTDR) and tetramethylrhodamine, ethyl ester (TMRE).[41–43] MTDR fluorescence can be processed by the MitoGraph software[44–47] to quantify features of the mitochondrial network (Figure 1D, features key and raw measurements). The TMRE fluorescence is proportional to mitochondrial transmembrane potential (TM-ψ) and, thus, electron transport system (ETS) activity.

Raw MitoGraph outputs are processed into metrics that describe mitochondrial morphology in single cells (Figure 1D, derived metrics). The “MitoGraph fusion score” (FUS) quantifies the relative contribution of fusion to steady-state morphology. Likewise, the “MitoGraph fission score” (FIS) quantifies the contribution of fission. FUS forms the numerator and FIS the denominator for the MitoGraph connectivity score (MCS), which quantifies network complexity. Finally, the MitoGraph heterogeneity score (MHS) quantifies the intracellular heterogeneity of mitochondrial morphology.

MitoSinCe^2 analyses of mnCF and mnCM mitochondria revealed largely expected differences, though with significant cell-to-cell variability within each group (Figure 1E). mnCMs contained significantly more mitochondria with more nodes and edges. Additionally, the nodes were higher order, with more 4-way junctions and fewer free ends (Figure 1F). mnCM mitochondria also showed expectedly higher TM-ψ (Figure 1G) and total mitochondrial length and volume, indicating higher mitochondrial mass. Unexpectedly, mnCMs had lower average mitochondrial width (Figure 1H). This conflicts with more reliable measurements obtained from electron microscopy[48] and is, thus, likely an artifact of MitoGraph skeletonization of densely packed CM mitochondria.

The unique CM mitochondrial structure also revealed limitations in FIS, FUS, and MCS. mnCMs showed a higher proportion of total mitochondrial length contained in the largest discreet element (fusion1) and a trend toward higher branching complexity (average [avg.] degree). Despite this, we found no difference in FUS because the average edge length was lower in mnCMs (Figure 1I), a consequence of the grid-like organization of IFMs. For the same reason, the number of edges normalized to total length (norm. edges) was higher in mnCMs, which led to slightly higher FIS (and lower MCS). The other components of FIS showed a trend toward lower mitochondrial numbers normalized by total length (fission) and no change to nodes normalized by total length (norm. nodes) (Figures 1J and 1K). Finally, MHS was higher in mnCMs, which we expected due to the sharp distinction between IFMs and peripheral mitochondria (Figure 1L).

Altogether, despite the limitations of published summary metrics in this system, the expected trends of higher abundance, interconnectedness, and energetics within mnCM mitochondrial networks compared to those of mnCFs are clear. Based on our observations, as a cell transitions from a CF toward a CM-like phenotype, a reprogrammed iCM with mature mitochondria should show increases in basal and ATP-linked respiration and an increase in mitochondrial mass, fusion, organizational complexity, and TM-ψ.

Characterization of mitochondrial energetics and morphology during cardiac reprogramming

To describe the degree to which the mitochondria in a given cell are CM-like or CF-like, we designed mitochondrial identity (ID) scores. We selected five metrics for a CM score (fusion1, norm. edges, 4-way junctions, MHS, and TM-ψ) and four for a CF score (fission, avg. width, avg. edge length, and free ends). We combined CF and CM scores into a reprogramming score. Plotting these scores showed effective segregation of mnCFs and mnCMs (Figure 2A).

We next induced cardiac reprogramming in freshly isolated mnCFs (Figures S2A and S2B). We then performed MST at reprogramming weeks 1, 2, and 5 alongside matched mnCF controls and mnCMs at week 1. Basal, ATP-linked, and ROS-linked OCRs remained largely stable for mnCMs between 2 and 7 days in culture, but the spare capacity at week 1 showed a highly significant increase over matched mnCF controls. Reprogramming wells showed higher basal, ATP-linked, and ROS-linked OCRs by reprogramming week 2 that continued through week 5. Basal and ATP-linked OCRs never reached the levels of mnCMs, while proton leak reached CM levels by week 2 and surpassed them by week 5. In contrast, spare capacity never showed an increase over controls (Figures 2B and 2C).

We applied MitoSinCe[2] analyses to reprogramming, which allowed us to normalize mitochondrial OCR by the average total length of mitochondrial networks for each condition (Figure S3A). Week 1 mnCMs showed higher OCRs per μm of mitochondria per cell than matched mnCFs. Additionally, this difference does not appear in reprogramming cells until reprogramming week 5, at which point the basal and reserve OCR/μm_{mt}/cell matches that for mnCMs. We then immunostained MST wells for CM marker cardiac troponin T (cTnT) and found high and significant positive correlations between OCR values and %cTnT+ cells,

particularly for basal and ATP-linked OCR (Figure S3B). Altogether, these data suggest that cardiac reprogramming increases mitochondrial respiration over time.

We then characterized mitochondria during reprogramming with MitoSinCe[2] metrics and mitochondrial ID scores. By reprogramming day 7 (Figure 2D), we saw no significant changes in mitochondrial content (mito. content) (Figure 2E), but we observed significant reductions in CF score metrics (Figure 2F) and increases in three of the CM score metrics: norm. edges, 4-way junctions, and MHS. Fusion1 showed a trend toward increase, but TM-ψ decreased, consistent with MST results (Figure 2G). Despite this, mitochondrial ID scores suggest significant shifts from CF-like to CM-like mitochondria at day 7 (Figure S3C). Based on the distribution in mnCFs, we set reprogramming score of ≥2 as indicative of reprogramming. A higher proportion of MGT-transduced cells (35%) pass this point than mnCFs (7.5%) (Figure 2H).

We saw increases in mito. content by reprogramming days 10 and 14, though the length and volume of mitochondria in mnCFs also increased at day 14 (Figure S3E). Avg. width and avg. edge remained lower in reprogramming cells, while fission and free ends were higher (Figure S3F). We saw no significant differences in fusion1 or 4-way junctions at these time points but did see higher norm. edges and MHS. TM-ψ was still lower in reprogramming cells at day 10 but was significantly higher by day 14 (Figure S3G). For both time points, ~20% of cells registered as reprogramming by mitochondrial ID scores compared to ~14% of mnCF controls (Figures S3H and S3I).

By reprogramming day 29 (Figure 2I), MGT-transduced cells showed no significant difference from mnCFs in mito. content. However, reprogramming cells showed a bimodal distribution with distinct high and low populations (Figure 2J). We saw renewed reduction in fission and free ends, no difference in avg. edge, and an increase in avg. width (Figure 2K). Of the CM score metrics, only 4-way junctions significantly increased, but as with mito. content, each metric showed increases at the upper ends of their distributions (Figure 2L). Though several of these shifts in distribution were not significant using the Kolmogorov-Smirnov test, they contributed to the mitochondrial ID scores registering 25% of cells as reprogramming compared to 4.5% of mnCF controls (Figures 2M and S3D),

We next performed transmission electron microscopy (TEM) at reprogramming week 6 to investigate mitochondrial ultrastructure in CFs vs. iCMs (Figure 2N). The low n of cells for these experiments warrants caution in their interpretation, but we note a few striking findings. In comparison to CF mitochondria, iCM mitochondria were, on average, ~2-fold larger by area and showed ~15% higher cristae density. However, while reprogramming cells showed evidence of formation of sarcomeric structures, we found no examples of obvious intrafibrillar integration of mitochondria (Figures 2O and S3J). Finally, we saw increased expression of mitochondrial fusion and mitochondrially encoded genes at reprogramming week 2 compared to CF controls (Figure 2P), suggestive of mitochondrial biogenesis.

Together, these results indicate that cardiac reprogramming induces a metabolic shift toward mitochondrial energetics. Our data suggest a time course for mitochondrial change during cardiac reprogramming. During week 1, reprogramming factors induce fusion to more

highly branched networks without increasing mitochondrial energetics. By the end of week 2, nascent iCMs increase mitochondrial biogenesis, leading to increased respiration per cell. Only by later time points do mitochondria increase in energetic efficiency complete with high branching and denser cristae (Figure 2Q). The relative incompleteness of the shift to CM-like mitochondria led us to hypothesize that the switch to mitochondrial energy is rate limiting for conversion to mature iCMs. We next investigated whether perturbing mitochondrial dynamics impacts cardiac reprogramming.

Mitochondrial fusion is critical for iCM conversion, while fission regulator Mtfr1l is a major barrier

As a proof of concept, we screened small-molecule inhibitors of the mitochondrial fission effector dynamin-related protein 1 (DRP1) (mDivi-1,[49] p110,[50] and Dynasore[51]), OPA1 (Myls22[52]), and MFN1/2 (MF18[53] and 5-fluorouracil[54]) for their impact on reprogramming (Figure S4A). Of the fission inhibitors, only p110, the peptide inhibitor of DRP1 recruitment to mitochondria, increased the yield of iCMs (~1.4-fold) (Figure S4B). However, all three fusion inhibitors ablated reprogramming (~5-, ~2.5-, and ~15-fold, respectively) (Figure S4C).

We next performed a loss-of-function (LoF) screen of regulators of mnCF[55] mitochondrial dynamics during reprogramming using lentiviral short hairpin RNA (shRNA) constructs. After confirming efficient knockdown (Figure S4D), we evaluated iCM conversion at reprogramming day 10 using flow cytometry for the CM markers cTnT and α-Actinin (ACTN2) (Figures 3A and S4E). In keeping with our pilot experiments, the loss of *Opa1*, *Mfn1*, and *Mfn2*[13] impaired iCM conversion. In addition, the pro-fission *Mtfr1l* emerged as a potent reprogramming barrier (Figures 3A and 3B). Each individual shRNA targeting *Mtfr1l* improved reprogramming, but the mix of three shRNAs showed the highest iCM yield (~5-fold over control) (Figures 3C, S4F, and S4G). For further experiments, therefore, we used the sh*Mtfr1l*-mix (denoted sh*Mtfr1l*), which also led to a significant loss of MTFR1L protein (Figure S4H). Finally, the loss of *Mtfr1l* increased iCM conversion, regardless of the reprogramming day we added sh*Mtfr1l*, within the first week (Figures S5A–S5C).

We next investigated the functional maturity of the nascent iCMs obtained from MGT-sh*Mtfr1l* and MGT-shNT. The expression of various CM markers increased in MGT-sh*Mtfr1l* compared to MGT-shNT (Figure 3D). The increase in CM marker expression between shNT and sh*Mtfr1l* was highest (~3- to 4-fold) at reprogramming day 7 (Figures S5D–S5H). Encouragingly, sh*Mtfr1l* led to an ~8-fold increase in the area of spontaneously beating loci (Figures 3E; Videos S1 and S2) and ~7-fold more cells exhibiting calcium cycling (Figures 3F; Videos S3 and S4). Finally, we investigated the impact of sh*Mtfr1l* on cardiac reprogramming in other fibroblast types. Notably, sh*Mtfr1l* increased cardiac reprogramming efficiency by ~3-fold in mouse embryonic fibroblasts (MEFs) (Figures S5I and S5J) and ~2-fold in freshly isolated (Figure S5K) murine adult CFs (maCFs) (Figures S5L and S5M).

Together, these results indicate that mitochondrial fusion is required for successful cardiac reprogramming. Inhibition of mitochondrial fission had mixed impacts but broadly increased

iCM conversion efficiency, particularly with loss of the fission regulator *Mtfr1l*. In reprogramming murine fibroblasts, the knockdown of *Mtfr1l* led to increases (~5-fold in mnCFs, ~3-fold in MEFs, and ~2-fold in maCFs) in cells expressing CM markers and in functionally mature iCMs (~7- to 8-fold in mnCFs). We next investigated the mitochondrial phenotypes associated with MGT-sh*Mtfr1l* iCMs.

Loss of Mtfr1l alters the mitochondria of putative iCMs to more closely resemble those of mnCMs

To characterize mitochondrial structure and function after perturbation, we began by knocking down mitochondrial dynamics genes in mnCFs. At knockdown day 3, we compared mitochondrial morphology and membrane potential. Qualitatively, each knockdown altered mitochondrial morphology as expected (Figure S6A), but the impacts of each knockdown on mitochondrial membrane potential were modest (Figure S6B). As such, we then focused our attention on reprogramming with or without sh*Mtfr1l*.

MST at reprogramming week 2 revealed a ~25% increase in basal and ATP-linked OCRs along with a ~50% increase in proton leak in the MGT+sh*Mtfr1l* cells compared to the MGT+shNT control (Figure 4A). When normalized to the average total length of the mitochondrial network for each condition, the percentage of increase was doubled for each rate per mm of mitochondria (Figure S6C). This suggests that the loss of *Mtfr1l* leads to an earlier or more robust change in mitochondrial energetics toward a more CM-like phenotype by reprogramming week 2.

We next performed MitoSinCe[2] comparing cells reprogrammed with MGT+shNT or sh*Mtfr1l* at reprogramming week 2 (Figure 4B). In keeping with MST results, the loss of *Mtfr1l* pushed mitochondrial structure-function in reprogramming cells toward more CM-like phenotypes. Of the mito. content metrics (Figure 4C), total length and volume showed no significant change, while mito. number reduced ~30% with sh*Mtfr1l*. This means that similar mitochondrial mass is incorporated into fewer, larger networks, which is reflected in the CF score metrics (Figure 4D). MGT-sh*Mtfr1l* cells showed decreases in fission and free ends. Conversely, avg. edge and avg. width showed significant increases. For the CM score metrics (Figure 4E), fusion1 and 4-way junctions were higher in MGT-sh*Mtfr1l* relative to MGT-shNT, while the norm. edges metric was lower.

All these differences are reflective of inhibited fission,[46] but they suggest that by week 2 of reprogramming, the mitochondria of the knockdown cells have not adopted the unique CM-like structure and density that shift the edge and width metrics counterintuitively. Finally, MHS and TM-ψ also showed significant increases (~1.4-fold) in sh*Mtfr1l* over control, reflecting higher intracellular heterogeneity and ETS activity, respectively. Combining these results into mitochondrial CF, CM, and reprogramming scores (Figures S6E and 4F), the CM-like population (reprogramming score^{3}2) is ~4.67-fold higher in the knockdown than the control, roughly in keeping with the relative reprogramming efficiencies from flow and immunofluorescence (IF) experiments (Figures 3B and 3C).

We next investigated the impact of sh*Mtfr1l* on sarcomere organization. Putative iCMs in both control and knockdown groups showed organized sarcomeres alternating ACTN2

and cTnT (Figures 4C, left, and S6F, top left). We then costained sarcomeric proteins and mitochondria with either MTDR or the IMM protein HSP60, which is essential for cardiac function[56] (Figures 4C, left, and S6F, top middle). Both control and knockdown reprogramming conditions gave rise to cells with alternating cTnT and HSP60, indicating the incorporation of mitochondria into sarcomeres (Figure S6F, top right).

We quantified mitochondrial-sarcomere integration in whole cells using Manders overlap coefficients (MOCs). We calculated MOCs for cTnT and ACTN2 (Figure S6F, bottom left), cTnT and HSP60 (Figure S6F, bottom right), ACTN2 and MTDR (Figure 4C, top right), and cTnT and MTDR (Figure 4C, bottom right). *Mtfr1l* knockdown cells showed significantly higher overlap between ACTN2 and cTnT, primarily because of the higher proportion of double-positive cells. We found no significant differences between shNT and sh*Mtfr1l* MOCs for sarcomeric protein overlap with mitochondria. Interestingly, the reverse overlap, that of mitochondria with sarcomeric protein, diverged: HSP60 showed ~30% less overlap with cTnT in the knockdown cells, while MTDR showed ~1.5- and ~2-fold higher overlaps with ACTN2 and cTnT, respectively. Because HSP60 localizes to the IMM, we investigated mitochondrial ultrastructure in knockdown and control reprogramming cultures.

We performed TEM on MGT+shNT and MGT+*Mtfr1l* at reprogramming weeks 2 and 6. We analyzed the mitochondrial pools of 5 cells for each condition at reprogramming week 2 and of 9 cells for each condition at week 6. At week 2, mitochondria and their cristae were significantly larger in the knockdown cells than controls. However, the cristae density was significantly lower in the knockdown (Figure 4D). This difference at reprogramming week 2 may explain the divergence between HSP60's (IMM) and MTDR's (whole organelle) overlaps with sarcomeric proteins. By week 6, the difference in average mitochondrial area was ablated, but MGT+sh*Mtfr1l* mitochondria showed ~25% higher cristae density on average. In keeping with this, MGT-sh*Mtfr1l* increased the expression of fusion regulators and mitochondrially encoded genes, which code for ETS subunits and preferentially locate to cristae (Figure S6G).

Consistent with our flow cytometry, beating, and calcium flux assays, a qualitative analysis of our TEM images suggested that the sarcomeric structures were more completely formed in the *Mtfr1l* knockdown cells and that the same showed more intrafibrillar integration of mitochondria (Figure 4E). Moreover, the percentage of the cell area occupied by clear sarcomeric structures for each group was 14-fold higher in the knockdown. Together, our results demonstrate that loss of *Mtfr1l* markedly promotes CM-like mitochondrial phenotypes, leading to more functionally mature iCMs.

Loss of Mtfr1l primes CFs for cell fate conversion to iCMs mitigated by concomitant loss of Opa1

We next interrogated the mechanisms by which sh*Mtfr1l* increased iCM yield and shifted mitochondrial phenotypes. We performed bulk RNA sequencing (RNA-seq) of mnCFs and reprogramming cells at week 1 to compare control and knockdown cultures. Principal-component analysis (PCA) showed clear segregation of conditions and grouping of biological replicates (Figures S7A and S8A). Analysis of differentially expressed genes (DEGs) indicated relatively minor changes to gene expression in knockdown mnCFs (Figure

S7B) but robust differences in the transcriptomes of reprogramming groups (Figures S8B and S8C).

Loss of *Mtfr1l* in both mnCFs and reprogramming cells reduced expression of the actin polymerization regulator *Arpc2*, the ferritin heavy subunit *Fth1*, and the ER protein disulfide isomerase *Txndc5*. However, the differences in sh*Mtfr1l*-induced DEGs between mnCFs and reprogramming cells suggest that sh*Mtfr1l* impacts gene expression in concert with reprogramming factors. In mnCFs, sh*Mtfr1l* downregulated Gene Ontology (GO) terms for extracellular matrix (ECM) organization and connective tissue development and upregulated terms for atrial CM communication and ECM disassembly (Figures S7C and S7D). Gene set enrichment analysis (GSEA) yielded similar enriched terms along with terms for transport and utilization of calcium and other ions (Figures S7E–S7H). Loss of *Mtfr1l* may, therefore, prime fibroblasts for transdifferentiation to striated muscle.

GO enrichment analysis in reprogramming cells showed the expected sh*Mtfr1l*-induced upregulation of terms associated with cardiac development, calcium signaling, and muscle contraction. Additionally, there was further downregulation of genes related to fibroblast activity, including ECM formation, connective tissue development, and collagen metabolism (Figures S8D and S8E). Excitingly, GO and GSEA showed an upregulation of genes related to mitochondrial energetics and biogenesis and a downregulation of gene sets related to the ECM (Figures S8D–S8I).

We saw slight sh*Mtfr1l*-induced increases in the expression of *Mfn1* and *Mfn2* as well as the DRP1 recruiters *Mff* and *Mief2*. Simultaneous upregulation of fusion and fission genes may indicate compensation for the loss of *Mtfr1l* or enhanced mitochondrial turnover. Loss of the known *Mtfr1l* target[31] *Opa1* ablated reprogramming in our LoF screen. We thus explored how concomitant loss of *Opa1* impacted MGT+sh*Mtfr1l* reprogramming. After confirming the knockdown (Figure S9A), we evaluated reprogramming through RT-qPCR (Figure 5A), IF (Figure 5B), and flow cytometry (Figure 5C) for CM markers. The loss of both genes mitigated the impact of the loss of one, suggesting shared regulation.

Comparing transcriptomes of cultures expressing MGT with sh*Mtfr1l*, sh*Opa1*, both, or shNT revealed distinct clusters of DEGs (Figure 5D). Three of these showed opposite expression patterns in sh*Mtfr1l* and sh*Opa1* that were reverted in sh*Mtfr1l*+sh*Opa1*. Genes in clusters 3 (Figure 5E) and 4 (Figure 5F) were largely downregulated in sh*Mtfr1l* and upregulated in sh*Opa1*. Both clusters were enriched for GO terms for translation regulation and mitochondrial apoptotic signaling. Interestingly, GSEA of these clusters showed that gene sets related to the ribosome and nitric oxide biosynthesis were up- and down-regulated, respectively, in sh*Mtfr1l*, and vice versa in sh*Opa1* (Figure S9B, left and middle). Other enriched terms in cluster 3 related to fibrosis and oxidative stress, while those in cluster 4 related to stress pathways and ketone metabolism.

Cluster 7 (Figure 5G) genes were upregulated in sh*Mtrf1l*, downregulated in sh*Opa1*, and included enriched terms for cardiac development, mitophagy, and energy regulation. Additionally, GSEA showed marked upregulation of the gene sets involved in TM transport of inorganic ions (Figure S9B, right). Thus, where the loss of *Mtfr1l* weakens fibroblast

identity and promotes mitochondrial energetics, loss of *Opa1* inhibits the acquisition of CM fate and induces fibrotic activity and mitochondrial stress.

We next evaluated the impact of the loss of *Opa1* and *Mtfr1l* on mitochondria at reprogramming week 2 (Figure 5H). As expected, the loss of *Opa1* led to the loss of mito. content (Figure 5I), hyperfission, and membrane depolarization (Figures 5J and 5K). The double knockdown reverted every metric toward non-targeting controls. This includes, to a lesser extent, the mitochondrial ID scores (Figures S9C and 5L). Hypothesizing that reduced *Mtfr1l*-induced *Opa1* cleavage might increase the iCM yield, we explored the OPA1 protein in MEFs (Figure S9D) expressing shNT or sh*Mtfr1l*. Loss of *Mtfr1l* led to a slight but significant increase in the OPA1-l:OPA1-s ratio. Finally, DRP1 protein levels (like *Dnm1l* expression) were unchanged.

Our sequencing and rescue results collectively demonstrate that the loss of *Mtfr1l* significantly induces the loss of fibroblast identity, promotes mitochondrial energetics, and facilitates the acquisition of CM identity. We explored a potential link to the fusion regulator *Opa1* from the literature and showed that the loss of *Opa1* effectively counters the loss of *Mtfr1l*. We like-wise link metabolic reprogramming to cardiac reprogramming. We propose a model wherein promoting fusion and cristae reorganization increases mitochondrial respiration and lowers energetic barriers to iCM conversion.

Using machine learning for prediction of reprogramming in live cells by mitochondrial phenotypes

Our next question was whether we could identify reprogramming cells using mitochondrial metrics without fixation or genetically encoded lineage-tracing fluorophores.[57] The study and clinical translation of cardiac regenerative medicine will benefit from novel tools to evaluate reprogramming in live cells. The correlation of our reprogramming scores with IF and flow assessments hinted that such a strategy might be feasible. We, therefore, built a machine learning model trained to identify reprogramming cells from their mitochondria. In uniform manifold approximation and projection (UMAP) plots combining all MitoGraph and MitoSinCe[2] metrics, MGT-expressing cells cluster more closely with mnCMs than do their matched mnCF controls (Figure 6A, top). Additionally, MGT+sh*Mtfr1l* cells cluster more closely with one of the mnCM clusters than do MGT+shNT, MGT+sh*Opa1*, or MGT+sh*MO* (Figure 6A, bottom).

Each metric had distinct correlations with other metrics (Figure 6B) and with the outcome of CF or CM (Figure 6C). Using these correlations and our understanding of CF and CM mitochondria, we built a model based on FIS, MHS, and TM-ψ (Figure 6D). We trained the model on the mnCFs and mnCMs and tested a version lacking TM-ψ on fixed cTnT+ cells. The model performed well on both the training and test datasets (Figure 6E), so we applied both versions (with and without TM-ψ) to our experimental datasets. The version without TM-ψ lacked predictive power compared with flow and IF evaluations of efficiency. Including TM-ψ yielded predictions matching the trends of other assays (Figure 6F). To refine the model to reliably identify individual cells as putative iCMs will require CM lineage-tracing models to assess reprogramming in live cells, which can be stained with TMRE. However, as far as we are aware, this is the first attempt to evaluate reprogramming

using the proxy of mitochondrial morphology and energetics, and our results show promise for future iterations.

DISCUSSION

We investigated changes to mitochondria during reprogramming from fibroblasts to iCMs. We began with a baseline comparison of mitochondria in mnCFs and mnCMs. Expectedly, mnCMs showed higher basal, ATP-linked, ROS-linked, and maximal mitochondrial OCRs. mnCM mitochondrial networks also showed higher fusion, lower fission, and a more negative TM-ψ. Using this baseline, we evaluated mitochondria over a reprogramming time course. We found that ROS-linked OCRs, mitochondrial content, fusion, and TM-ψ shift toward CM-like phenotypes by reprogramming week 2. However, other metrics, including OCR/mm_{mt}, cristae density, and sarcomere integration, change later or never (Figure 6G).

We therefore screened regulators of mitochondrial dynamics for their impacts on reprogramming. We found that mitochondrial fusion is required for iCM conversion. Importantly, we also found that the loss of *Mtfr1l* induced CM-like mitochondrial phenotypes earlier in reprogramming and increased the yield of mature iCMs. Transcriptome analysis revealed that the loss of *Mtfr1l* weakens fibroblast identity, increases mitochondrial energetics, and upregulates markers of mature CMs. The simultaneous loss of *Opa1* countered each of these shifts. We propose that sh*Mtfr1l*-facilitated cardiac reprogramming is fusion dependent. The loss of *Mtfr1l* promotes mitochondrial fusion, cristae reorganization, and mitochondrial energetics and primes cells for reprogramming to iCMs.

AMPK-dependent activation of MTFR1L promotes the proteolytic cleavage of OPA1 to its fusion-deficient short form. We saw a slight increase in the OPA1-l:OPA1-s ratio, but it is unlikely to completely account for the robust changes induced by *Mtfr1l* knockdown. It remains possible that the primary mechanism involves a direct link to OPA1 activity. Changes to gene expression suggest that the loss of *Mtfr1l* increases, while the loss of *Opa1* decreases, translation and ion transport but, respectively, decreases and increases oxidative stress. Because the double knockdown mitigated each of these changes, they may suggest potential mechanisms for sh*Mtfr1l*-facilitated iCM conversion. Indeed, we recently showed that loss of the translation repressor *Ybx1* can facilitate cardiac reprogramming with a single factor.[28]

Conversely, the mechanism may merely depend on functional fusion and, thus, require *Opa1* along with *Mfn1/2*. *Mtfr1l*'s published roles in cristae organization, iron storage, and mitochondrial localization may also contribute to its function as a reprogramming barrier. Additionally, because *Mtfr1l* loss weakens fibroblast identity, its further study will yield insights into fibroblast biology in health and disease. Finally, *Mtfr1l* may be a barrier in reprogramming toward multiple lineages, impacting regenerative medicine more broadly.

Of the seven genes whose knockdown promoted cardiac reprogramming, six (*Mtfr1l*, *Inf2*, *Tmem135*, *Parl*, *Fis1*, and *Dnm1l*/DRP1) are known to promote mitochondrial fission. Additionally, *Mtfr1l* and *Parl* can both participate in OPA1 cleavage. The seventh (*Chchd3*/MIC19) is part of the mitochondrial contact site and cristae organizing system (MICOS)

complex and mediates OMM and IMM interactions. Its loss leads to swelling of the mitochondrial matrix.[58] It, too, directly interacts with OPA1 to stabilize cristae junctions and mediate communication between OPA1 and the OMM. Interestingly, it can be cleaved by OMA1, one of the major effectors of OPA1 cleavage, and its short form disrupts cristae stability, OMM-IMM contact sites, and mitochondrial respiration. While we did not follow up on these other hits from our screen, they tell a consistent story that inhibition of mitochondrial fission, promotion of fusion, and facilitation of cristae reorganization are beneficial to iCM conversion and maturation.

Another innovation of our work is the proof of concept for evaluating reprogramming in live cells using mitochondrial metrics without fixation or genetically encoded lineage-tracing tools. Machine learning is emerging as a powerful tool for image analysis, and our model's predictions matched the trends of traditional assessments, predicting the emergence of reprogramming cells by reprogramming week 2. With further refinement, this model could be invaluable for the evaluation of reprogramming in real time while allowing for further experiments on the same cells.

The present manuscript describes the in-depth characterization of mitochondrial structure-function relationships during cardiac reprogramming. Combining MitoSinCe^2 with machine learning techniques will also allow for the characterization of intracellular mitochondrial heterogeneity. In the cardiac field, this could lead to a more detailed understanding of mitochondrial structure-function relationships of IFMs vs. peripheral mitochondria. Finally, this study identifies *Mtfr1l* as a potent barrier to cardiac reprogramming, highlighting its role in the maintenance of CF identity.

Limitations of the study

In this study, we quantify mitochondrial morphology and function in live single cells using mitochondrially targeted fluorescent dyes and confocal microscopy. Our characterization was, therefore, limited by the 3D spatial resolution of these techniques. The inadequacy of published metrics to describe the densely packed CM mitochondrial networks (described above) is a direct consequence of this limitation. Additionally, the relatively low throughput of our SinCe^2 analyses meant our study lacked the statistical power to identify rare sub-populations within each condition. This limitation is compounded for our study because our target cells, nascent iCMs, make up only 5%–30% of the population of cells, depending on the reprogramming condition. Future studies making use of lineage-tracing tools may usefully refine the results presented herein. Low throughput also ultimately led to our decision to focus on membrane potential as our sole functional metric in single-cell experiments. Future studies incorporating different functional probes (mitochondrial ROS, matrix ATP, etc.) will provide a more detailed picture of how mitochondrial function changes during reprogramming. Additionally, our experiments were performed on cardiac cells isolated from a mixed population of male and female mice, and thus, we can make no determination as to the impact of sex on mitochondrial rearrangement during cardiac reprogramming. Finally, our work suggests multiple potential mechanisms for sh*Mtfr1l* facilitating iCM conversion and hints at underlying regulatory pathways that remain to be fully explored.

RESOURCE AVAILABILITY

Lead contact

Further information and requests for resources and reagents should be directed to the lead contact, Li Qian (li_qian@med.unc.edu).

Materials availability

Reagents used in this study that are not commercially available can be shared upon reasonable request following submission of a materials transfer agreement.

Data and code availability

- All data generated or analyzed during this study are included in this published article (and its supplemental information files).
- Bulk RNA-seq data are available from the NCBI Gene Expression Omnibus (GEO) and are publicly available as of the date of publication. The accession number is listed in the key resources table.
- Microscopy data reported in this paper will be shared by the lead contact upon request.
- Any additional information required to reanalyze the data reported in this paper is available from the lead contact upon request.

STAR★METHODS

EXPERIMENTAL MODEL AND STUDY PARTICIPANT DETAILS

Animal Handling—All experiments involving animals were performed in accordance with the University of North Carolina at Chapel Hill (UNC Chapel Hill) Institutional Animal Care and Use Committee (24–110), which conforms to the NIH Guidelines for the Care and Use of Laboratory Animals. Wildtype CD1 mice were purchased from Charles River (CD1 ISD) and maintained by the Division of Comparative Medicine Facility at UNC Chapel Hill. Mice were maintained with controlled temperature and light/dark cycles with standardized chow, bedding, caging and daily inspection. CD1 lines were maintained by breeding one 3–6 month old male and two 3–6 month old females.

MEF—Mouse embryonic fibroblasts (MEFs) were isolated from CD1 embryos at embryonic day 13.5 as previously described.[27] In brief, following decapitation and red organ removal, embryos were mechanically and enzymatically dissociated with Collagenase II (Worthington #LS004177). The cell suspension was passed through a 40 μm nylon mesh, cultured to confluence on plates pre-coated with 0.1% gelatin in 1X DPBS, trypsinized, passed through a 40 μm nylon mesh, and frozen at P1. MEFs were thawed and cultured in CF media (Iscove's Modified Dulbecco's Medium (IMDM), 20% FBS, 1% Penicillin/Streptavidin) for all experiments when used. Cells were not directly tested for mycoplasma contamination. However, Hoechst staining did not reveal the presence of mycoplasma genomes.

Mouse cardiac fibroblast—Cardiac fibroblasts were isolated from neonates as previously described.[27] Briefly, neonatal hearts were collected from wildtype P0-P3 CD1 pups, mechanically dissociated with a razor, and pooled into a 50 mL conical tube. Prewarmed 0.05% Trypsin-EDTA was added at 10 mL per 20 hearts and incubated for 10 min in a 37°C water bath. Once the tissue settled, the supernatant was aspirated, and the tissue pieces were resuspended in 0.5 mg/mL Collagenase II in 1X HBSS and incubated at 37°C for 5 min. After 5 min, the conical tube is vortexed for 30 s, the dissociated cells in the supernatant are removed and added to CF media (Iscove's Modified Dulbecco's Medium (IMDM), 20% FBS, 1% Penicillin/Streptavidin). The collagenase step was repeated 4–6 more times and the dissociated cells in the supernatant were pooled together. The pooled cells were filtered through a 40 μm mesh strainer and the flowthrough was centrifuged at 300 x*g* for 5 min. The resulting cell pellet was prepared for MACS sorting with biotinylated anti-Thy1 antibody to enrich for neonatal Thy1+ CFs as previously described.[27,70] Following MACS sorting, the CFs were resuspended in CF media and plated in wells pre-coated with 0.1% gelatin in 1X DPBS. We performed IF and flow cytometry for CF the marker vimentin to evaluate isolation efficiency. Over 90% of cells retained after mnCF isolation were vimentin+. (Figures S1A–S1C) Adult cardiac fibroblasts were isolated from 3–4-month-old CD1 adults as previously described (CITE GF Nature Comm paper). Briefly, adult hearts were collected from 2 male and 2 female wildtype 3–4-month-old CD1 mice, mechanically dissociated with a razor, enzymatically digested in a Collagenase solution (1 mg/mL Collagenase II + 1 mg/mL Collagenase IV (Worthington #LS0004189) in HBSS), and incubated for 30 min at 37°C with vortexing every 5 min. The cells were filtered through a 40 μm mesh strainer and the flowthrough was centrifuged at 400 x *g* for 10 min. The supernatant was removed, and the pellet was resuspended in ACK Lysis Buffer (5 mL per heart; ThermoFisher #A1049201), and incubated at room temperature for 5 min. Finally, the cells were centrifuged at 400 x *g* for 10 min for 10 min, resuspended in CF media and plated in wells pre-coated with 0.1% gelatin in 1X DPBS for 4 h. The CF media was replaced with new CF media to wash away cell debris after 4 h. Once confluent (~4 days), the CFs were seeded (20,000 cells/well) directly onto gelatin-coated Seahorse 96-well plates (Agilent) and 8-well live cell microscopy chambers (IBIDI). Over 90% of cells retained after maCF isolation were vimentin+. (Figure S5K) All experiments using adult CFs were conducted 48h after seeding. Cells were not directly tested for mycoplasma contamination. However, Hoechst staining did not reveal the presence of mycoplasma genomes.

Mouse cardiomyocyte—CMs were isolated from neonatal hearts from wildtype P0-P3 CD1 pups. To do so, we used the Worthington Neonatal Cardiomyocyte Isolation System (Worthington Biochemical Corporation, LK003300) according to modified manufacturer's protocols. Following CM enrichment by differential centrifugation, we retained the supernatant cells and followed the procedure outlined above for isolating CFs to compare CFs and CMs from the same heart. Cells from the pellet were seeded (40,000 cells/well) directly onto 0.1% gelatin-coated 24-well plates (Corning) in iCM media ((DMEM/M199(4:1), 10% FBS, 1% penicillin/streptomycin) at 37°C and 5%CO_2 in a humidified incubator for 90 m. After this initial incubation, wells were gently flushed with the supernatant media using a 1 mL micropipet and the supernatant was re-seeded (20,000 cells/well) directly onto 0.1% gelatin-coated Seahorse 96-well plates (Agilent) and 8-well

live cell microscopy chambers (IBIDI) and cultured in iCM media at 37°C and 5%CO_2 in a humidified incubator. We performed IF and flow cytometry (see below) for CM markers to evaluate isolation efficiency. Our mnCM isolation yielded cells ~70% positive for cTnT and ACTN2 (Figures S1D–S1F). All experiments for isolated CMs were conducted 48 h or 7 d after seeding. Cells were not directly tested for mycoplasma contamination. However, hoechst staining did not reveal the presence of mycoplasma genomes.

METHOD DETAILS

Viral packaging—HEK 293T (ATCC, CRL-3216) and HEK 293T platE (Cell Biolabs, RV-101) cells were cultured in DMEM with 10% FBS, 1% non-essential amino acids and 1% penicillin/streptomycin. Cells were not tested for mycoplasma contamination. Lentiviruses were packaged in 29T3 by co-transfection with 10 μg lentiviral DNA plasmids, 7 μg psPAX2, and 3 μg pMD2.G with Lipofectamine 2000 (ThermoFisher) according to manufacturer instructions. Murine MGT retroviruses were packaged in platE by transfection with 15 μg pMx-puro-MGT. Fresh media was added 12h after transfection. Viral supernatants were collected at 48 and 72h after transfection, filtered through 0.45 μm filters and incubated with 8% PEG-4000 at 4°C overnight. Viral particles were centrifuged at 4000 rpm for 20 min at 4°C, and then resuspended with DMEM. Retrovirus was used freshly and lentivirus either freshly or frozen at −80°C for future use. Lentiviral shRNA plasmids are from Sigma and Table S1 includes a list of shRNA oligos for the non-targeting construct and the 22 candidate genes used in our LOF screen. Selected genes are annotated with GO terms related to mitochondrial fission or fusion and expressed in mnCFs.[55] A pool of two to three independent shRNAs targeting different regions of each gene were expressed simultaneously at Reprogramming Day 1. Efficient knockdown was confirmed with RT-qPCR (Figure S4D) and iCM conversion efficiency evaluated at Reprogramming Day 10 using flow cytometry for cTnT and ACTN2. (Figures 3A and S4E).

Direct reprogramming of CFs to iCMs—Murine fibroblasts were reprogrammed according to previously reported protocols.[28] MEFs, neonatal fibroblasts and adult fibroblasts isolated from CD1 mice were seeded (40,000 cells/well) in a gelatin-coated 24-well plate with CF media. One day after seeding (defined as D0), cells were transfected with fresh 48h retrovirus and 4 μg/mL polybrene (EMD Millipore, TR-1003-G) in iCM media to initiate reprogramming. Media was changed 24 h after retroviral infection at D1 and 72h retrovirus was added along with small molecule inhibitors or 48h + 72h lentivirus as noted. Small molecule inhibitors of mitochondrial fission used in this screen included mDivi-1[49] (0.25mM; Sigma), p110[50] (0.25μM; Tocris) and Dynasore[51] (0.25mM; Sigma). Those for mitochondrial fusion included Myls22[52] (0.5mM; MedChem Express), MF18[53] (0.5mM; MedChem Express) and 5-fluorouracil[54] (0.5mM; Sigma). From Day 2 to Day 14, cells were cultured iCM media and the medium (including small molecule inhibitors where noted) was replaced every other day. Cells were harvested for analysis at labeled time points. To assess spontaneous beating with calcium imaging traces, iCM medium was replaced by beating media (Stempro-34 SF medium, 1x GlutaMax, 50 mg/mL L-Ascorbic acid, 5 ng/mL recombinant human VEGF-165, 10 ng/mL recombinant human FGF-basic, 50 ng/mL recombinant human FGF-10) on Day 14.[28]

Mitochondrial stress test—All metabolic flux analysis was performed on the Seahorse XFe96 platform (Agilent). For measurements comparing between CMs and CFs, CMs and CFs were isolated from the same heart and directly seeded (20,000 cells/well) onto gelatin-coated Seahorse 96-well plates (Agilent) and 8-well live cell microscopy chambers (IBIDI). For measurements between reprogramming and control cells, cells were resuspended as single cells using acutase (5 m, 37 C, 5% CO_2) and then seeded (20,000 cells/well) in a gelatin-coated Seahorse 96-well. All mitochondrial stress tests and metabolic flux analysis was performed 48 h after seeding. Non-mitochondrial respiration was obtained by measuring oxygen consumption rate (OCR) after Antimycin A (2μM, Sigma) and Rotenone (2μM, Millipore Sigma) addition. Basal respiration was obtained by subtracting non-mitochondrial OCR from OCR. Proton leak was obtained by subtracting non-mitochondrial OCR from OCR after Oligomycin (10μM, Sigma) addition. Maximal respiration was obtained by subtracting non-mitochondrial OCR from the OCR achieved after Carbonyl Cyanide *m*-Chlorophenylhydrazone (CCCP; 2μM, Sigma) addition as titrated. Spare capacity was obtained as the difference between the maximal and basal respiration. Immediately after experimentation, cells were stained for 20 m at RT with Hoechst 33342 solution in 1X PBS (1:10,000 dilution; ThermoFisher) and each well was imaged using an EVOS fluorescence microscope. Nuclei in each well were counted using FIJI with manual thresholding to normalize OCR values. All bioenergetic profiling was performed with normalized OCR values.[40] To obtain correlation between OCRs and proportion of CM-like cells, MST wells were PFA fixed, immunostained for cTnT before EVOS imaging (see: immunofluorescence microscopy).

MitoSinCe^2 analysis with confocal microscopy—Cells were seeded (cell count/well) in gelatin-coated 8-well live cell chambers (IBIDI). Cells were co-stained with MitoTracker Deep Red (MTDR; 0.5 Invitrogen) and Tetramethylrhodamine Ethyl Ester Perchlorate (TMRE; 100nM; Sigma) as previously described.[71] Confocal microscopy was performed on an Andor Dragonfly Spinning Disc Confocal Microscope using the proprietary Andor software. Confocal micrographs were acquired using an HC PL APO 63X/1.4 Oil objective and a Zyla Plus 4.2MP sCMOS camera with 1.5X zoom. We used 561nm (TMRE) and 637nm (MTDR) lasers with optimized laser powers, pixel dwell and appropriate filters to minimize crosstalk, cross-excitation and bleaching. Live cells were imaged using a temperature and CO_2 controlled chamber set to 37°C and 5% CO_2. Raw images were processed using FIJI and custom macros. Briefly, images were converted to tiffs, the MTDR and TMRE channels were split, and the instrument background (93 AU) was subtracted from all images. Maximum intensity z-projections were obtained, and those for the MTDR channel were used to manually draw ROIs around individual cells in each image. The ROI sets were then used to cut out individual cells from the 3D MTDR images and to obtain TMRE MFI from the z-projected TMRE images. From the latter, image-specific background fluorescence was obtained with standard ROIs and subtracted to correct raw TMRE MFI values. MTDR stains actively respiring mitochondria in an otherwise function-independent manner. This function-independent fluorescence channel was processed by the MitoGraph v3.0 software[44–47] with default thresholding. QC was performed by comparing binary z-projections of the mitochondrial elements recognized by MitoGraph for each cell to its raw image. MitoGraph quantified features of the mitochondrial network, including the

number of discreet mitochondrial elements in a cell, their nodes and edges and the type of junction at each node (free end, 3-way or 4-way) where edges branch off.[44] Additionally, the software measures the lengths, widths and volumes of individual mitochondria and the total network. From the raw outputs, we derived validated metrics and scores to quantify mitochondrial morphology in single cells. The "MitoGraph Fusion Score" (FUS) combines metrics linked to fusion activity—the length of the largest contiguous mitochondrial network as a proportion of the Total Length, the average length of all edges in the cell, and a weighted average of the type of junction at each node (Fusion1, Avg. Edge Length and Avg. Degree)—to quantify the relative contribution of the fusion apparatus to steady-state morphology. Likewise, the "MitoGraph Fission Score" (FIS) quantifies the contribution of fission activity by combining the total numbers of discreet mitochondria, nodes and edges recognized by MitoGraph normalized to the Total Length (Fission, Norm. Nodes and Norm. Edges). FUS and FIS form the numerator and denominator, respectively, for the MitoGraph Connectivity Score (MCS), a metric of relative network complexity. Finally, the MitoGraph Heterogeneity Score (MHS) combines the standard deviations of the raw metrics for individual mitochondria and the Average Degree to quantify intracellular heterogeneity of mitochondrial morphology. (Figure 1D)[41,42,45,46]

RT-qPCR and RNA-seq—Total RNA was extracted from reprogramming and control cultures at the labeled time points with TRIzol (Invitrogen) using manufacturer's protocol. The RNA pellet was resuspended in RNase-free water for further analysis. For RT-qPCR, purified RNA was reversed transcribed into cDNA using Super Script IV Reverse Transcriptase (Invitrogen). RT-qPCR was performed to quantitatively detect mRNA levels using SYBR Green PCR Master Mix (Thermofisher) on Applied Biosystems QuantStudio6 real-time PCR system (Thermofisher). Primers pairs used for RT-qPCR are listed in Table S1. For bulk RNA-sequencing, total RNA (1ug) was sent to NovoGene for sequencing library preparation and high throughput sequencing of Poly-A selected RNAs using Illumina's NovaSeq XPlus series PE150 platform. Quality control was performed using FastQC. Reads were aligned to the mouse MM10_UCSC reference genome using BBMap,[60] and only uniquely mapped reads were retained. Gene expression was inferred using featureCounts and subsequent analysis to obtain DEGs were performed in R using DESeq2. Gene ontology, gene set and KEGG enrichment analyses were performed in R using clusterProfiler and GSEABase.

Flow cytometry—Cells were fixed, permeabilized and stained with the BD Biosciences Fixation/Permeabilization Kit. Briefly, cells grown in a 24-well plate were washed with PBS, trypsinized (5 m), quenched with 1:1 iCM media, and transferred into a 96-well suspension plate. Cell pellets were collected through centrifugation and resuspended in 1X fixation/permeabilization solution for 30 min at 4°C. After incubation, cells were washed twice with 1X permeabilization/wash solution, stained with primary antibody diluted in 1X permeabilization/wash solution for 30 min at 4°C, washed once with 1X permeabilization/wash solution, stained with secondary antibody diluted in 1X permeabilization/wash solution for 30 min at 4°C, and lastly washed once with 1X permeabilization/wash solution. Cells were then resuspended in PBS and evaluated with an Attune NxT Flow Cytometer (Thermofisher). Gating was performed in the forward and side scatter channels to remove

debris and doublet cells. FCS files were exported and analyzed using FlowJo. Primary antibodies and relevant dilutions were as follows: anti-cTnT, 1:500 (Invitrogen, MA5-12960) and sarcomeric αActinin (Abcam, AB68167). Secondary antibodies and relevant dilutions are as follows: Alexa Fluor 488 anti-mouse, 1:500 (Jackson Immunoresearch, 715-545-150) and Alexa Fluor 647 anti-rabbit, 1:500 (Jackson Immunoresearch, 711-605-152).

Immunofluorescence Microscopy—Immunofluorescence staining was performed as previously described.[72,73] In brief, cells were washed with twice with 1X PBS, fixed with 4% PFA in 1X PBS for 15 min, washed twice with 1X PBS, permeabilized with 0.1% Triton X-100 in 1X PBS for 15 min, blocked with 5% BSA in 1X PBS for 1 h, stained overnight with primary antibody diluted in 1% BSA in 1X PBS, washed three times with 1X PBS, stained with secondary antibody diluted in 1% BSA in 1X PBS for 1 h, washed once with 1X PBS, stained for 30 s with Hoechst 33342 solution in 1X PBS (1:10,000 dilution; ThermoFisher), and lastly washed thrice with 1X PBS. Samples were imaged in air at RT using an EVOS fluorescence microscope equipped with 4x, 10x, 20x and 40x objectives and configured with laser/filter combinations for DAPI, GFP, RFP, Cy5 and transmitted light. Primary antibodies and relevant dilutions are as follows: anti-cTnT, 1:400 (Invitrogen, MA5-12960); anti-sarcomeric α-Actinin, 1:500 (Abcam, AB68167); and anti-Hsp60, 1:500 (Cell Signaling, 12165). Secondary antibodies and relevant dilutions are as follows: Alexa Fluor 488 anti-mouse, 1:500 (Jackson Immunoresearch, 715-545-150) and Alexa Fluor 647 anti-rabbit, 1:500 (Jackson Immunoresearch, 711-605-152). All staining was performed at room temperature unless otherwise indicated.

Mitochondria sarcomere incorporation analysis—High-resolution 3D images (xy = 0.064μm, z = 0.2um) were acquired for IF stained samples using an Andor Dragonfly Spinning Disk Confocal Microscope. Confocal micrographs were acquired using an HC PL APO 63X/1.4 Oil objective and a Zyla Plus 4.2MP sCMOS camera with 1.5X zoom. We used 405nm (Hoechst), 488nm (cTnT/ACTN2), 561nm (cTnT) and 637nm (ACTN2/HSP60/MTDR) lasers with optimized laser powers, pixel dwell and appropriate filters to minimize crosstalk, cross-excitation and bleaching. Images were processed in FIJI to obtain maximum intensity projections of 8 z-slices (covering ~1.4um) showcasing regularly organized sarcomere structures. Alternating cTnT (for sarcomeric structures) and Hsp60 (for mitochondria) fluorescence intensity was measured in FIJI using linear ROIs drown along and perpendicular to sarcomeric structures. Once obtained, fluorescence intensity normalized to max fluorescence was plotted over the length of the ROI in Microsoft Excel. To co-stain for cTnT, ACTN2 and MTDR, live cells were stained with MTDR at 37°C for 15 min followed directly by PFA fixation and IF. Manders' Overlap Coefficients were obtained in FIJI using whole cell ROIs and the BiOP plug-in with automated Otatsu thresholding.

Calcium imaging traces—Calcium imaging was performed as previously described.[28] In brief, reprogramming cells were cultured for 2 weeks in reprogramming media followed by 4 weeks in beating media and subsequently stained with 1x Calbryte 590 (AAT Bioquest) working solution. The dye-loaded samples were incubated in the dark at 37°C 5% CO_2 for 1 h. Cells were washed three times in HBSS to remove excess probe. Spontaneous calcium cycling videos were taken using an EVOS fluorescence microscope with a 20x objective and

the configuration for RFP. Calcium transients were analyzed using FIJI by selecting calcium signal positive clusters, and measuring the peak amplitude expressed relative to the baseline fluorescence between action potentials (F/F0).

Transmission electron microscopy—Freshly isolated mnCF controls were cultured for 6 weeks in optimized fibroblast media and reprogramming cells for 2 or 6 weeks (4 weeks in reprogramming media followed by 2 weeks in beating media) as noted. Cells were monitored by brightfield microscopy. On appearance of spontaneously beating loci, cellular monolayers were fixed with 2% paraformaldehyde/2.5% glutaraldehyde in 0.15 M sodium phosphate buffer, pH 7.4 for 1 h at room temperature and stored in fixative at 4°C. For Transmision Electron Microscopy (TEM) processing, cells were washed three times with 0.15 M sodium phosphate buffer for 10 min and then incubated with 1% osmium tetroxide in 0.15 M sodium phosphate for 1 h. Cells were washed three times with deionized water and dehydrated through an ascending ethanol series (30%, 50%, 75%, 90%, 100%, 100% 100%). Cells were infiltrated with three exchanges (1 h, overnight for ~16 h, and 6 h) of Polybed 812 epoxy resin (Polysciences, Inc., Warrington, PA). Next cells were embedded in fresh 100% Polybed 812 epoxy resin and allowed to cure at 60°C until hardened. Resin blocks were sectioned at 80 nm using a diamond ultra knife (DiATOME, 30-US) on a Leica UCT7 ultramicrotome and mounted on 200 mesh copper grids (EMS, T200H-Cu). Grids were stained with 4% aqueous uranyl acetate (EMS, 22400-4) for 12 min followed by Reynold's lead citrate for 8 min (Reynolds, 1963). Samples were viewed using a JEOL JEM-1230 transmission electron microscope operating at 80 kV (JEOL USA, Inc., Peabody, MA) and images were obtained using a Gatan Orius SC1000 CCD Digital Camera and Gatan Microscopy Suite 3.0 software (Gatan, Inc., Pleasanton, CA). MnCFs were selected for imaging at random while reprogramming cells were selected based on the presence of gap junctions, (proto-)sarcomeric structures or T-tubules. Cells in shRNA experiments were also selected based on presence of lentiviral particles. Mitochondrial and cristae area, cristae density and sarcomere area were quantified using FIJI.

Western blot—Cell lysates were incubated in cold RIPA Buffer (ThermoFisher #89900) supplemented with PhosStop (Roche) and complete EDTA-free Protease Inhibitor cocktail (Roche) for 15 min at 4°C. The resulting supernatant was collected, and the protein concentration was measured using Lowry Assay (Biorad #5000111). The lysates were mixed with Lamelli loading buffer at the same protein concentration and heated to 100°C for 10 min. Protein samples were then subjected to SDS-polyacrylamide gel electrophoresis on a 4%–20% acrylamide gel (Biorad, #4561096) and transferred to a nitrocellulose membrane. Membranes were rinsed with TBST (20mM Tris 150mM NaCl and 0.1% Tween 20) and blocked with 5% BSA in TBST at room temperature for 1 h. Membranes were incubated with primary antibody in 5% BSA in TBST overnight at 4°C. Blots were washed three times with TBST for 5 min at room temperature, incubated with horseradish peroxidase-conjugated (HRP) secondary antibody for 1 h at room temperature, and washed three times with TBST for 5 min at room temperature. Blots were developed with a chemiluminescent reagent (SuperSignal West Pico PLUS #34579) and imaged on a ChemiDoc (BIORAD). Target protein band intensity was quantified using FIJI. Primary antibodies and relevant dilutions are as follows: anti-DRP1, 1:1000 (Cell Signaling, 5391S); anti-OPA1, 1:1000

(Cell Signaling, 80471S); anti-MTFRL1, 1:250 (Invitrogen, PA5-55516), and anti-bActin, 1:10000 (Santa Cruz, sc-37778). HRP secondary antibodies and relevant dilutions are as follows: Donkey-*anti*-Mouse HRP, 1:2500 (Jackson Immunoresearch, #715-035-150); and Donkey-*anti*-Rabbit HRP 1:2500 (Jackson Immunoresearch, #711-035-152).

Machine learning model to evaluate reprogramming using mitochondrial metrics—Data preprocessing and feature selection for the model is based on the following criteria where the train data is the mitochondrial features of native CMs and CFs and the test set is iCMs. Features unrelated to the prediction task were removed. The selected features for the models were 'MitoGraph Fission Score' and MitoGraph Heterogeneity Score' with and without 'TM-ψ'. These features were standardized using the StandardScaler (scikit-learn 1.5.1)[68] to ensure each feature had a mean of zero and a standard deviation of one. To address class imbalance, the Synthetic Minority Over-sampling Technique (SMOTE) from the imbalanced-learn library 0.12.4[64] was applied to the training data, generating synthetic samples for the minority class. Two different machine learning models were trained using the standardized features: a Random Forest classifier (scikit-learn 1.5.1) and an XGBoost classifier (Xgboost 2.1.1).[69] The XGBoost classifier was selected for evaluation as it is more robust to different time points and scenarios. Hyperparameter tuning for the XGBoost model was performed using GridSearchCV (scikit-learn 1.5.1), which involved a grid search over predefined hyperparameter values with cross-validation on train data. The model was evaluated by performance metrics such as precision, recall, and F1-score. Our goal was to optimize model parameters to improve recall, focusing on robustness in identifying the minority class. The most predictive hyperparameters were identified, and the resulting model was evaluated on the test set. Confusion matrices for the training and test sets were computed to evaluate the performance of the best model in terms of true positive, true negative, false positive, and false negative predictions. We visualized the data by Uniform Manifold Approximation and Projection (UMAP) separated by shRNA groups and time using matplotlib 3.9.2.[65] The correlation between each feature and the outcome was calculated using the point-biserial correlation coefficient. A heatmap of the correlation matrix was generated to visualize the relationships. The data processing and matrix calculation was completed using Numpy[66] and Pandas.[67]

QUANTIFICATION AND STATISTICAL ANALYSIS

No statistical method was used to predetermine sample size. The sample sizes were determined based on our previous experience and literature conducting similar experiments to achieve statistical differences between groups.[27,74,75] All samples were entered into the study in a randomized order. Investigators were blinded to the sample groups during data collection and analysis. GraphPad Prism software (version10) was used for statistical analysis. All data is presented as mean ± SEM of three or more biological replicates unless otherwise indicated in the figure legend. Differences between groups were examined for statistical significance using two-tailed Student's t test to compare means or the Kolmogorov-Smirnov test to compare distributions for paired groups, or one-way ANOVA with Tukey's comparisons test (adjusted p value) to compare means or the Kruskal-Wallis test followed by Dunn's Test to compare distributions for multiple groups. The specific test

for each experiment is noted in the figure legend. For statisctial significance * indicates $p < 0.05$, ** $p < 0.01$, *** $p < 0.001$ and **** $p < 0.0001$.

Supplementary Material

Refer to Web version on PubMed Central for supplementary material.

ACKNOWLEDGMENTS

We would like to thank all members of the Qian and Liu labs for their thoughtful comments and suggestions. BioRender was used to prepare our graphical abstract. We would also like to acknowledge UNC-CH's Flow Cytometry Core (North Carolina Biotech Center Institutional Support Grant 2017-IDG-1025, NIH 1UM2AI30836-01, and NIH/NCBI P30CA016086); the Microscopy Services Laboratory (NIH/NCBI P30CA016086 and NIH S10OD030223), especially Pablo Ariel, Kristen White, and Jillann Madren; and the Nutrition Obesity Research Center (NIH/NIDDK P30DK056350), especially Qing Shi and Erika Rezeli. Additionally, Megan Harwig, Blake Hill, Sandeep Sarangi, and Matheus Viana helped with troubleshooting for MitoGraph. This work was funded by NIH/National Heart, Lung, and Blood Institute 1F32HL176045-01 (B.M.S.), R35HL155656 (L.Q.), R01HL139976 (J.L.), R01HL139880 (J.L.), and 1K99HL175039-01 (Y.X.); American Heart Association Postdoctoral Fellowships 24POST1199447 (B.M.S.) and 23POST1026377 (Y.X.); American Heart Association Predoctoral Fellowship 23PRE1019178 (S.N.R.); and American Heart Association grants 20EIA35310348 (L.Q.) and 20EIA35320128 (J.L.).

REFERENCES

1. Tan CMJ, and Lewandowski AJ (2020). The transitional heart: from early embryonic and fetal development to neonatal life. Fetal Diagn. Ther 47, 373–386. 10.1159/000501906. [PubMed: 31533099]
2. Thomas D, Cunningham NJ, Shenoy S, and Wu JC (2022). Human-induced pluripotent stem cells in cardiovascular research: current approaches in cardiac differentiation, maturation strategies, and scalable production. Cardiovasc. Res 118, 20–36. 10.1093/cvr/cvab115. [PubMed: 33757124]
3. Bae J, Salamon RJ, Brandt EB, Paltzer WG, Zhang Z, Britt EC, Hacker TA, Fan J, and Mahmoud AI (2021). Malonate promotes adult cardiomyocyte proliferation and heart regeneration. Circulation 143, 1973–1986. 10.1161/CIRCULATIONAHA.120.049952. [PubMed: 33666092]
4. Honkoop H, de Bakker DE, Aharonov A, Kruse F, Shakked A, Nguyen PD, de Heus C, Garric L, Muraro MJ, Shoffner A, et al. (2019). Single-cell analysis uncovers that metabolic reprogramming by ErbB2 signaling is essential for cardiomyocyte proliferation in the regenerating heart. Elife 8, e50163. 10.7554/eLife.50163. [PubMed: 31868166]
5. Emelyanova L, Bai X, Yan Y, Bosnjak ZJ, Kress D, Warner C, Kroboth S, Rudic T, Kaushik S, Stoeckl E, et al. (2021). Biphasic effect of metformin on human cardiac energetics. Transl. Res 229, 5–23. 10.1016/j.trsl.2020.10.002. [PubMed: 33045408]
6. Guo Y, Lei I, Tian S, Gao W, Hacer K, Li Y, Wang S, Liu L, and Wang Z (2019). Chemical suppression of specific C-C chemokine signaling pathways enhances cardiac reprogramming. J. Biol. Chem 294, 9134–9146. 10.1074/jbc.RA118.006000. [PubMed: 31023824]
7. Wang J, Gu S, Liu F, Chen Z, Xu H, Liu Z, Cheng W, Wu L, Xu T, Chen Z, et al. (2022). Reprogramming of fibroblasts into expandable cardiovascular progenitor cells via small molecules in xeno-free conditions. Nat. Biomed. Eng 6, 403–420. 10.1038/s41551-022-00865-7. [PubMed: 35361933]
8. Bektik E, Sun Y, Dennis AT, Sakon P, Yang D, Deschenes I, and Fu J-D (2021). Inhibition of CREB-CBP Signaling Improves Fibroblast Plasticity for Direct Cardiac Reprogramming. Cells 10, 1572. 10.3390/cells10071572. [PubMed: 34206684]
9. Garry GA, Bezprozvannaya S, Chen K, Zhou H, Hashimoto H, Morales MG, Liu N, Bassel-Duby R, and Olson EN (2021). The histone reader PHF7 cooperates with the SWI/SNF complex at cardiac super enhancers to promote direct reprogramming. Nat. Cell Biol 23, 467–475. 10.1038/s41556-021-00668-z. [PubMed: 33941892]

10. Papadopoli D, Pollak M, and Topisirovic I (2021). The role of GSK3 in metabolic pathway perturbations in cancer. Biochim. Biophys. Acta. Mol. Cell Res 1868, 119059. 10.1016/j.bbamcr.2021.119059. [PubMed: 33989699]
11. Miao S, Zhao D, Wang X, Ni X, Fang X, Yu M, Ye L, Yang J, Wu H, Han X, et al. (2020). Retinoic acid promotes metabolic maturation of human Embryonic Stem Cell-derived Cardiomyocytes. Theranostics 10, 9686–9701. 10.7150/thno.44146. [PubMed: 32863954]
12. Glancy B, and Balaban RS (2021). Energy metabolism design of the striated muscle cell. Physiol. Rev 101, 1561–1607. 10.1152/physrev.00040.2020. [PubMed: 33733879]
13. Spurlock B, Tullet J, Hartman JL, and Mitra K (2020). Interplay of mitochondrial fission-fusion with cell cycle regulation: Possible impacts on stem cell and organismal aging. Exp. Gerontol 135, 110919. 10.1016/j.exger.2020.110919. [PubMed: 32220593]
14. Ngo J, Choi DW, Stanley IA, Stiles L, Molina AJA, Chen P-H, Lako A, Sung ICH, Goswami R, Kim M-Y, et al. (2023). Mitochondrial morphology controls fatty acid utilization by changing CPT1 sensitivity to malonyl-CoA. EMBO. J 42, e111901. 10.15252/embj.2022111901. [PubMed: 36917141]
15. Kondadi AK, and Reichert AS (2024). Mitochondrial dynamics at different levels: from cristae dynamics to interorganellar cross talk. Annu. Rev. Biophys 53, 147–168. 10.1146/annurev-biophys-030822-020736. [PubMed: 38166176]
16. Lu X, Thai PN, Lu S, Pu J, and Bers DM (2019). Intrafibrillar and perinuclear mitochondrial heterogeneity in adult cardiac myocytes. J. Mol. Cell. Cardiol 136, 72–84. 10.1016/j.yjmcc.2019.08.013. [PubMed: 31491377]
17. Willingham TB, Ajayi PT, and Glancy B (2021). Subcellular specialization of mitochondrial form and function in skeletal muscle cells. Front. Cell Dev. Biol 9, 757305. 10.3389/fcell.2021.757305. [PubMed: 34722542]
18. Kim Y, Ajayi PT, Bleck CKE, and Glancy B (2022). Three-dimensional remodelling of the cellular energy distribution system during postnatal heart development. Philos Trans R Soc Lond, B, Biol Sci 377, 20210322. 10.1098/rstb.2021.0322. [PubMed: 36189814]
19. Tsao CW, Aday AW, Almarzooq ZI, Anderson CAM, Arora P, Avery CL, Baker-Smith CM, Beaton AZ, Boehme AK, Buxton AE, et al. (2023). Heart disease and stroke statistics 2023 update: A report from the American Heart Association. Circulation 147, e93–e621. 10.1161/CIR.0000000000001123. [PubMed: 36695182]
20. Sadahiro T, and Ieda M (2022). In vivo reprogramming as a new approach to cardiac regenerative therapy. Semin. Cell. Dev. Biol 122, 21–27. 10.1016/j.semcdb.2021.06.019. [PubMed: 34210577]
21. Jain R, Poleshko A, and Epstein JA (2018). Beating the odds: programming proliferation in the mammalian heart. Genome Med. 10, 36. 10.1186/s13073-018-0550-5. [PubMed: 29776422]
22. Ko T, and Nomura S (2022). Manipulating cardiomyocyte plasticity for heart regeneration. Front. Cell Dev. Biol 10, 929256. 10.3389/fcell.2022.929256. [PubMed: 35898398]
23. Spurlock B, Liu J, and Qian L (2023). Can we stop one heart from breaking: triumphs and challenges in cardiac reprogramming. Curr. Opin. Genet. Dev 83, 102116. 10.1016/j.gde.2023.102116. [PubMed: 37797568]
24. Liu L, Guo Y, Li Z, and Wang Z (2021). Improving cardiac reprogramming for heart regeneration in translational medicine. Cells 10, 3297. 10.3390/cells10123297. [PubMed: 34943805]
25. Xie Y, Liu J, and Qian L (2022). Direct cardiac reprogramming comes of age: Recent advance and remaining challenges. Semin. Cell. Dev. Biol 122, 37–43. 10.1016/j.semcdb.2021.07.010. [PubMed: 34304993]
26. Wang Q, Spurlock B, Liu J, and Qian L (2024). Fibroblast reprogramming in cardiac repair. JACC. Basic Transl. Sci 9, 145–160. 10.1016/j.jacbts.2023.06.012. [PubMed: 38362341]
27. Wang H, Keepers B, Qian Y, Xie Y, Colon M, Liu J, and Qian L (2022). Cross-lineage potential of Ascl1 uncovered by comparing diverse reprogramming regulatomes. Cell Stem Cell 29, 1491–1504. 10.1016/j.stem.2022.09.006. [PubMed: 36206732]
28. Xie Y, Wang Q, Yang Y, Near D, Wang H, Colon M, Nguyen C, Slattery C, Keepers B, Farber G, et al. (2023). Translational landscape of direct cardiac reprogramming reveals a role of Ybx1 in repressing cardiac fate acquisition. Nat. Cardiovasc. Res 2, 1060–1077. 10.1038/s44161-023-00344-5. [PubMed: 38524149]

29. Jahng JWS, Zhang M, and Wu JC (2022). The role of metabolism in directed differentiation versus trans-differentiation of cardiomyocytes. Semin. Cell Dev. Biol 122, 56–65. 10.1016/j.semcdb.2021.05.018. [PubMed: 34074592]
30. Wang J-X, Jiao J-Q, Li Q, Long B, Wang K, Liu J-P, Li Y-R, and Li P-F (2011). miR-499 regulates mitochondrial dynamics by targeting calcineurin and dynamin-related protein-1. Nat. Med 17, 71–78. 10.1038/nm.2282. [PubMed: 21186368]
31. Tilokani L, Russell FM, Hamilton S, Virga DM, Segawa M, Paupe V, Gruszczyk AV, Protasoni M, Tabara L-C, Johnson M, et al. (2022). AMPK-dependent phosphorylation of MTFR1L regulates mitochondrial morphology. Sci. Adv 8, eabo7956. 10.1126/sciadv.abo7956. [PubMed: 36367943]
32. Andersson B, Wentland MA, Ricafrente JY, Liu W, and Gibbs RA (1996). A “double adaptor” method for improved shotgun library construction. Anal. Biochem 236, 107–113. 10.1006/abio.1996.0138. [PubMed: 8619474]
33. Yu W, Andersson B, Worley KC, Muzny DM, Ding Y, Liu W, Ricafrente JY, Wentland MA, Lennon G, and Gibbs RA (1997). Large-scale concatenation cDNA sequencing. Genome Res. 7, 353–358. 10.1101/gr.7.4.353. [PubMed: 9110174]
34. Novera W, Lee Z-W, Nin DS, Dai MZ-Y, Binte Idres S, Wu H, Damen JMA, Tan TZ, Sim AYL, Long YC, et al. (2020). Cysteine Deprivation Targets Ovarian Clear Cell Carcinoma Via Oxidative Stress and Iron-Sulfur Cluster Biogenesis Deficit. Antioxid. Redox Signal 33, 1191–1208. 10.1089/ars.2019.7850. [PubMed: 32336105]
35. Zheng X, Zhang C, Zheng D, Guo Q, Maierhaba M, Xue L, Zeng X, Wu Y, and Gao W (2022). An original cuproptosis-related genes signature effectively influences the prognosis and immune status of head and neck squamous cell carcinoma. Front. Genet 13, 1084206. 10.3389/fgene.2022.1084206. [PubMed: 36685880]
36. Virga DM, Hamilton S, Osei B, Morgan A, Kneis P, Zamponi E, Park NJ, Hewitt VL, Zhang D, Gonzalez KC, et al. (2024). Activity-dependent compartmentalization of dendritic mitochondria morphology through local regulation of fusion-fission balance in neurons in vivo. Nat. Commun 15, 2142. 10.1038/s41467-024-46463-w. [PubMed: 38459070]
37. Pellegrini L, and Scorrano L (2007). A cut short to death: Parl and Opa1 in the regulation of mitochondrial morphology and apoptosis. Cell. Death. Differ 14, 1275–1284. 10.1038/sj.cdd.4402145. [PubMed: 17464328]
38. Kang SWS, Cunningham RP, Miller CB, Brown LA, Cultraro CM, Harned A, Narayan K, Hernandez J, Jenkins LM, Lobanov A, et al. (2024). A spatial map of hepatic mitochondria uncovers functional heterogeneity shaped by nutrient-sensing signaling. Nat. Commun 15, 1799. 10.1038/s41467-024-45751-9. [PubMed: 38418824]
39. Janer A, Prudent J, Paupe V, Fahiminiya S, Majewski J, Sgarioto N, Des Rosiers C, Forest A, Lin Z-Y, Gingras A-C, et al. (2016). SLC25A46 is required for mitochondrial lipid homeostasis and cristae maintenance and is responsible for Leigh syndrome. EMBO Mol. Med 8, 1019–1038. 10.15252/emmm.201506159. [PubMed: 27390132]
40. Brand MD, and Nicholls DG (2011). Assessing mitochondrial dysfunction in cells. Biochem. J 435, 297–312. 10.1042/BJ20110162. [PubMed: 21726199]
41. Spurlock B, Gupta P, Basu MK, Mukherjee A, Hjelmeland AB, Darley-Usmar V, Parker D, Foxall ME, and Mitra K (2019). New quantitative approach reveals heterogeneity in mitochondrial structure-function relations in tumor-initiating cells. J. Cell. Sci 132, jcs230755. 10.1242/jcs.230755. [PubMed: 30910831]
42. Spurlock B, and Mitra K (2021). Mito-SinCe2 Approach to Analyze Mitochondrial Structure-Function Relationship in Single Cells. Methods. Mol. Biol 2275, 415–432. 10.1007/978-1-0716-1262-0_27. [PubMed: 34118054]
43. Spurlock B, Parker D, Basu MK, Hjelmeland A, Gc S, Liu S, Siegal GP, Gunter A, Moran A, and Mitra K (2021). Fine-tuned repression of Drp1-driven mitochondrial fission primes a “stem/progenitor-like state” to support neoplastic transformation. Elife 10, e68394. 10.7554/eLife.68394. [PubMed: 34545812]
44. Viana MP, Lim S, and Rafelski SM (2015). Quantifying mitochondrial content in living cells. Methods Cell Biol. 125, 77–93. 10.1016/bs.mcb.2014.10.003. [PubMed: 25640425]

45. Harwig MC, Viana MP, Egner JM, Harwig J, Widlansky ME, Rafelski SM, and Hill RB (2018). Imaging and quantifying mitochondrial morphology: a focus on the 3D freeware mitograph. FASEB. J 32, lb185. 10.1096/fasebj.2018.32.1_supplement.lb185.
46. Harwig MC, Viana MP, Egner JM, Harwig JJ, Widlansky ME, Rafelski SM, and Hill RB (2018). Methods for imaging mammalian mitochondrial morphology: A prospective on MitoGraph. Anal. Biochem 552, 81–99. 10.1016/j.ab.2018.02.022. [PubMed: 29505779]
47. Viana MP, Brown AI, Mueller IA, Goul C, Koslover EF, and Rafelski SM (2020). Mitochondrial fission and fusion dynamics generate efficient, robust, and evenly distributed network topologies in budding yeast cells. Cell Syst. 10, 287–297.e5. 10.1016/j.cels.2020.02.002. [PubMed: 32105618]
48. Collins HE, Kane MS, Litovsky SH, Darley-Usmar VM, Young ME, Chatham JC, and Zhang J (2021). Mitochondrial morphology and mitophagy in heart diseases: qualitative and quantitative analyses using transmission electron microscopy. Front. Aging 2, 670267. 10.3389/fragi.2021.670267. [PubMed: 35822027]
49. Cassidy-Stone A, Chipuk JE, Ingerman E, Song C, Yoo C, Kuwana T, Kurth MJ, Shaw JT, Hinshaw JE, Green DR, and Nunnari J (2008). Chemical inhibition of the mitochondrial division dynamin reveals its role in Bax/Bak-dependent mitochondrial outer membrane permeabilization. Dev. Cell 14, 193–204. 10.1016/j.devcel.2007.11.019. [PubMed: 18267088]
50. Qi X, Qvit N, Su Y-C, and Mochly-Rosen D (2013). A novel Drp1 inhibitor diminishes aberrant mitochondrial fission and neurotoxicity. J. Cell Sci 126, 789–802. 10.1242/jcs.114439. [PubMed: 23239023]
51. Macia E, Ehrlich M, Massol R, Boucrot E, Brunner C, and Kirchhausen T (2006). Dynasore, a cell-permeable inhibitor of dynamin. Dev. Cell 10, 839–850. 10.1016/j.devcel.2006.04.002. [PubMed: 16740485]
52. Chapa-Dubocq XR, Rodrıguez-Graciani KM, Garcıa-Báez J, Vadovsky A, Bazil JN, and Javadov S (2023). The Role of Swelling in the Regulation of OPA1-Mediated Mitochondrial Function in the Heart In Vitro. Cell 12, 2017. 10.3390/cells12162017.
53. Zou Y, Sun Y, Wang Y, Zhang D, Yang H, Wang X, Zheng M, and Shi B (2023). Cancer cell-mitochondria hybrid membrane coated Gboxin loaded nanomedicines for glioblastoma treatment. Nat. Commun 14, 4557. 10.1038/s41467-023-40280-3. [PubMed: 37507371]
54. Zhang D, and Ma J (2018). Mitochondrial Dynamics in Rat Heart Induced by 5-Fluorouracil. Med. Sci. Monit 24, 6666–6672. 10.12659/MSM.910537. [PubMed: 30240386]
55. Stone NR, Gifford CA, Thomas R, Pratt KJB, Samse-Knapp K, Mohamed TMA, Radzinsky EM, Schricker A, Ye L, Yu P, et al. (2019). Context-Specific Transcription Factor Functions Regulate Epigenomic and Transcriptional Dynamics during Cardiac Reprogramming. Cell Stem Cell 25, 87–102.e9. 10.1016/j.stem.2019.06.012. [PubMed: 31271750]
56. Fan F, Duan Y, Yang F, Trexler C, Wang H, Huang L, Li Y, Tang H, Wang G, Fang X, et al. (2020). Deletion of heat shock protein 60 in adult mouse cardiomyocytes perturbs mitochondrial protein homeostasis and causes heart failure. Cell Death Differ. 27, 587–600. 10.1038/s41418-019-0374-x. [PubMed: 31209364]
57. Sutcliffe MD, Tan PM, Fernandez-Perez A, Nam Y-J, Munshi NV, and Saucerman JJ (2018). High content analysis identifies unique morphological features of reprogrammed cardiomyocytes. Sci. Rep 8, 1258. 10.1038/s41598-018-19539-z. [PubMed: 29352247]
58. Yang S, Yin X, Wang J, Li H, Shen H, Sun Q, and Li X (2023). MIC19 exerts neuroprotective role via maintaining the mitochondrial structure in a rat model of intracerebral hemorrhage. Int. J. Mol. Sci 24, 11553. 10.3390/ijms241411553. [PubMed: 37511310]
59. Garbutt TA, Zhou Y, Keepers B, Liu J, and Qian L (2020). An optimized protocol for human direct cardiac reprogramming. STAR Protoc. 1, 100010. 10.1016/j.xpro.2019.100010. [PubMed: 32728671]
60. Bushnell B, Rood J, and Singer E (2017). BBMerge - accurate paired shotgun read merging via overlap. PLoS One 12, e0185056. 10.1371/journal.pone.0185056. [PubMed: 29073143]
61. Wu T, Hu E, Xu S, Chen M, Guo P, Dai Z, Feng T, Zhou L, Tang W, Zhan L, et al. (2021). clusterProfiler 4.0: A universal enrichment tool for interpreting omics data. Innovation 2, 100141. 10.1016/j.xinn.2021.100141. [PubMed: 34557778]

62. Love MI, Huber W, and Anders S (2014). Moderated estimation of fold change and dispersion for RNA-seq data with DESeq2. Genome. Biol 15, 550. 10.1186/s13059-014-0550-8. [PubMed: 25516281]

63. Morgan M, Falcon S, and Gentleman R (2023). GSEABase: *Gene set enrichment data structures and methods*. R package. 10.18129/b9.bioc.gseabase version 1.62.0.

64. Lemaıtre G, Nogueira F, and Aridas CK (2017). Imbalanced-learn: A Python Toolbox to Tackle the Curse of Imbalanced Datasets in Machine Learning. J. Mach. Learn. Res 18, 1–5.

65. Hunter JD (2007). Matplotlib: A 2D Graphics Environment. Comput. Sci. Eng 9, 90–95. 10.1109/MCSE.2007.55.

66. Oliphant TE (2006). Guide to NumPy, 1 (Trelgol Publishing).

67. McKinney W (2010). Data structures for statistical computing in python. In Proceedings of the 9th Python in Science Conference Proceedings of the python in Science Conference, van der Walt S, Millman J, eds. (SciPy), pp. 56–61. 10.25080/Majora-92bf1922-00a.

68. Pedregosa F, Varoquaux G, Gramfort A, Michel V, Thirion B, Grisel O, Blondel M, Prettenhofer P, Weiss R, Dubourg V, et al. (2011). Sci-kit-learn: Machine Learning in Python. J. Mach. Learn. Res 12, 2825–2830.

69. Chen T, and Guestrin C (2016). XGBoost: A Scalable Tree Boosting System. In Proceedings of the 22nd ACM SIGKDD International Conference on Knowledge Discovery and Data Mining - KDD '16, Krishnapuram B., Shah M., chairs (ACM Press), pp. 785–794. 10.1145/2939672.2939785.

70. Farber G, Dong Y, Wang Q, Rathod M, Wang H, Dixit M, Keepers B, Xie Y, Butz K, Polacheck WJ, et al. (2024). Direct conversion of cardiac fibroblasts into endothelial-like cells using Sox17 and Erg. Nat. Commun 15, 4170. 10.1038/s41467-024-48354-6. [PubMed: 38755186]

71. Mitra K, and Lippincott-Schwartz J (2010). Analysis of mitochondrial dynamics and functions using imaging approaches. Curr. Protoc. Cell Biol 46, 4–4.25.21. 10.1002/0471143030.cb0425s46.

72. Xie Y, Ma A, Wang B, Peng R, Jing Y, Wang D, Finnell RH, Qiao B, Wang Y, Wang H, and Zheng Y (2019). Rare mutations of ADAM17 from TOFs induce hypertrophy in human embryonic stem cell-derived cardiomyocytes via HB-EGF signaling. Clin. Sci 133, 225–238. 10.1042/CS20180842.

73. Xie Y, Wang Q, Gao N, Wu F, Lan F, Zhang F, Jin L, Huang Z, Ge J, Wang H, and Wang Y (2020). MircroRNA-10b Promotes Human Embryonic Stem Cell-Derived Cardiomyocyte Proliferation via Novel Target Gene LATS1. Mol. Ther. Nucleic Acids 19, 437–445. 10.1016/j.omtn.2019.11.026. [PubMed: 31902743]

74. Wang L, Ma H, Huang P, Xie Y, Near D, Wang H, Xu J, Yang Y, Xu Y, Garbutt T, et al. (2020). Down-regulation of Beclin1 promotes direct cardiac reprogramming. Sci. Transl. Med 12, eaay7856. 10.1126/scitranslmed.aay7856. [PubMed: 33087505]

75. Xie Y, Van Handel B, Qian L, and Ardehali R (2023). Recent advances and future prospects in direct cardiac reprogramming. Nat. Cardiovasc. Res 2, 1148–1158. 10.1038/s44161-023-00377-w. [PubMed: 39196156]

Highlights

- Direct cardiac reprogramming increases mitochondrial fusion and energetics
- Mitochondrial fusion is required for iCM conversion
- The mitochondrial fission regulator *Mtfr1l* is a potent reprogramming barrier
- Loss of *Mtfr1l* increases the yield of mature iCMs in a fusion dependent manner

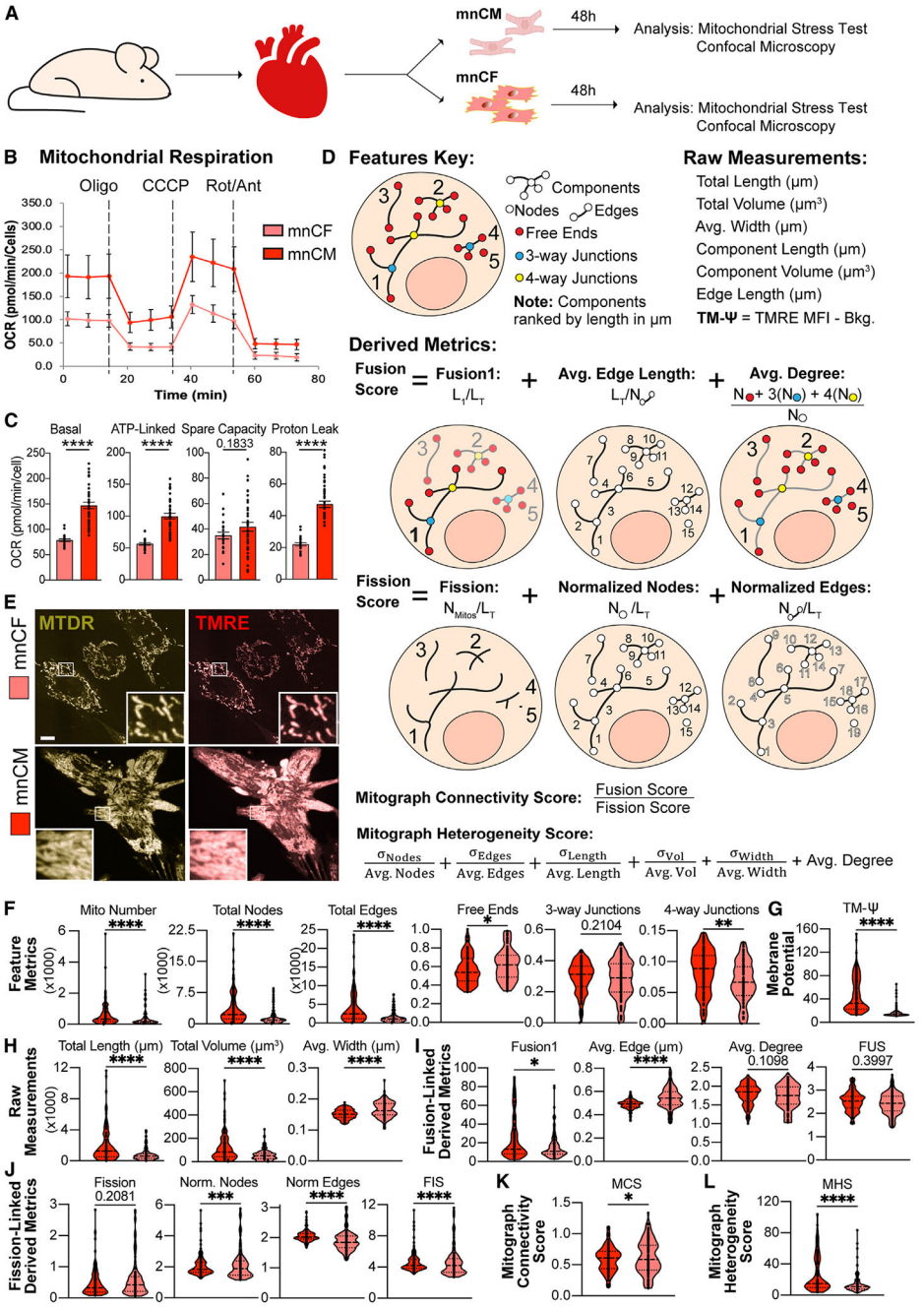

Figure 1. Direct quantitative comparison of the mitochondrial energetics and morphology of *ex vivo* murine neonatal CFs and CMs

(A) Experimental design for isolating and studying mnCFs and mnCMs.

(B) Line graph showing oxygen consumption rate (OCR) of mnCFs (n = 20) and mnCMs (n = 20) over time during a Seahorse mitochondrial stress test. Data are presented as mean ± SD; n is biological replicates.

(C) Bar graphs showing quantification of biologically meaningful mitochondrial energetics. From left to right: total basal mitochondrial OCR, OCR associated with generation of ATP, mitochondrial OCR above the basal rate cells could use to respond to new stimuli, and the

OCR associated with ETS proton leak and ROS generation. Data are presented as mean ± SEM; *n* is biological replicates Significance was determined by Student's t test (*n* = 20). **p* < 0.05, ***p* < 0.01, ****p* < 0.001, and *****p* < 0.0001.

(D) Description of metrics obtained from MitoSinCe^2 experiments.

(E) Representative micrographs of mnCF and mnCM mitochondria stained with MitoTracker Deep Red and TMRE. White boxes indicate zoomed-in regions. Scale bar: 5 μm.

(F) Violin plots showing quantification of SinCe^2 summary feature metrics for mnCFs (*n* = 119) and mnCMs (*n* = 125). Significance was determined by Kolmogorov-Smirnov test; *n* is cells. **p* < 0.05, ***p* < 0.01, ****p* < 0.001, and *****p* < 0.0001.

(G) Violin plot of the membrane potential between mnCFs (*n* = 119) and mnCMs (*n* = 125). Significance was determined by Kolmogorov-Smirnov test; *n* is cells. **p* < 0.05, ***p* < 0.01, ****p* < 0.001, and *****p* < 0.0001.

(H) Violin plots showing quantification of SinCe^2 raw mitochondrial measurements for mnCFs (*n* = 119) and mnCMs (*n* = 125). Significance was determined by Kolmogorov-Smirnov test; *n* is cells. **p* < 0.05, ***p* < 0.01, ****p* < 0.001, and *****p* < 0.0001.

(I) Violin plots showing quantification of fusion-linked derived metrics for mnCFs (*n* = 119) and mnCMs (*n* = 125). Significance was determined by Kolmogorov-Smirnov test; *n* is cells. **p* < 0.05, ***p* < 0.01, ****p* < 0.001, and *****p* < 0.0001.

(J) Violin plots showing quantification of fission-linked derived metrics for mnCFs (*n* = 119) and mnCMs (*n* = 125). Significance was determined by Kolmogorov-Smirnov test; *n* is cells. **p* < 0.05, ***p* < 0.01, ****p* < 0.001, and *****p* < 0.0001.

(K) Violin plot of MitoGraph connectivity score of mnCFs (*n* = 119) and mnCMs (*n* = 125). Significance was determined by Kolmogorov-Smirnov test; *n* is cells. **p* < 0.05, ***p* < 0.01, ****p* < 0.001, and *****p* < 0.0001.

(L) Violin plot of MitoGraph heterogeneity score of mnCFs (*n* = 119) and mnCMs (*n* = 125). Significance was determined by Kolmogorov-Smirnov test; *n* is cells. **p* < 0.05, ***p* < 0.01, ****p* < 0.001, and *****p* < 0.0001.

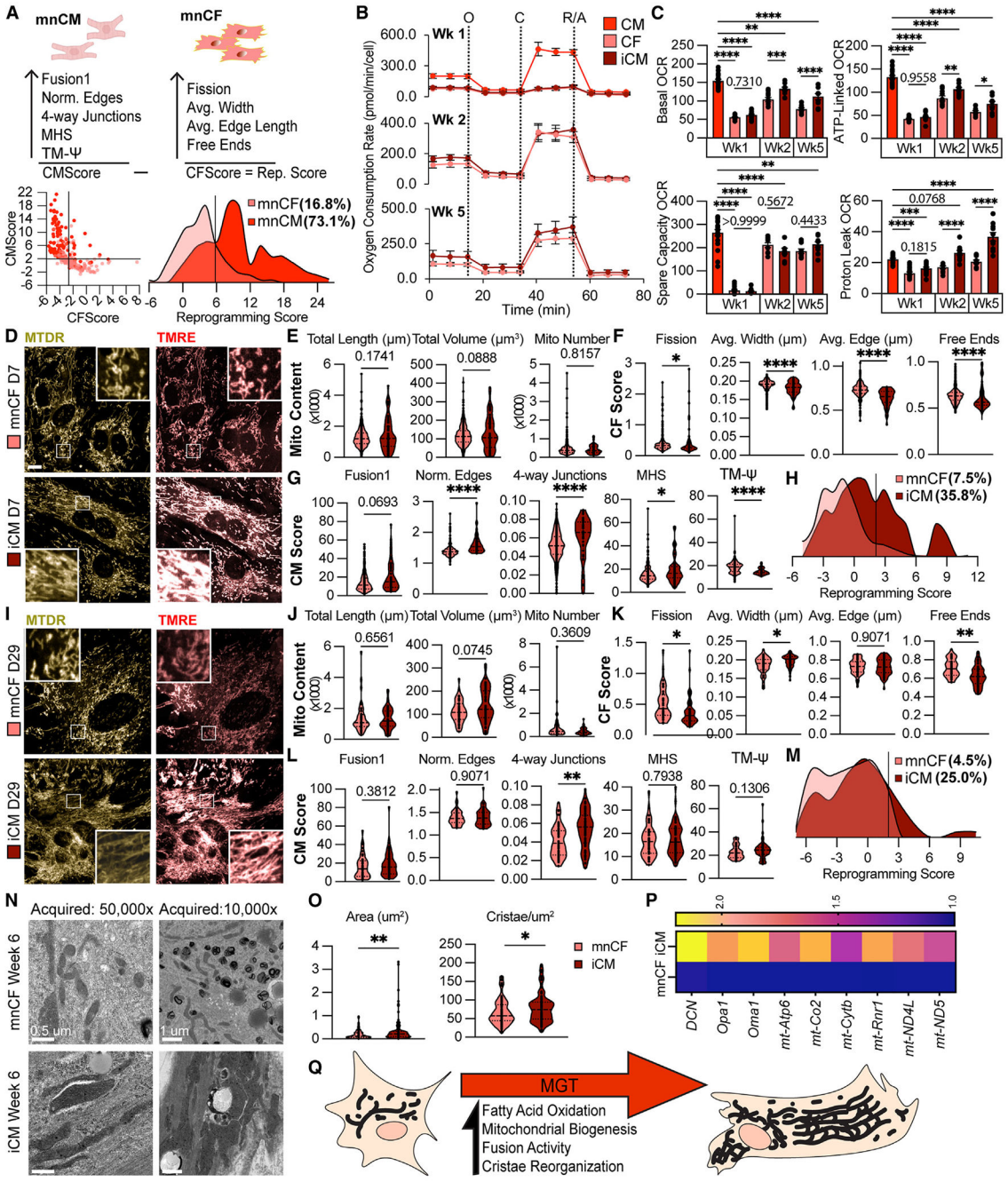

Figure 2. Characterization of mitochondrial energetics and morphology during cardiac reprogramming

(A) Schematic of parameters used to calculate mitochondrial ID scores with the cell-specific CF score and CM score against native mnCFs (n = 119) and mnCMs (n = 125), where n is cells.

(B) Line graphs showing oxygen consumption rates (OCRs) of control and cardiac reprogramming cultures during a Seahorse mitochondrial stress test over a reprogramming time course (week 1 n = 18–20, week 2 n = 10, and week 3 n = 10). Data are presented as mean ± SD; n is biological replicates.

(C) Bar graphs showing quantification of biologically meaningful mitochondrial energetics: OCR associated with generation of ATP, total basal mitochondrial OCR, mitochondrial OCR above the basal rate cells could use to respond to new stimuli, and the OCR associated with ETS proton leak and ROS generation. Data are presented as mean ± SEM; *n* is biological replicates. Significance was determined by one-way ANOVA followed by Sidak's test for multiple comparisons (week 1 $n = 18–20$, week 2 $n = 10$, and week 3 $n = 10$). *$p < 0.05$, **$p < 0.01$, ***$p < 0.001$, and ****$p < 0.0001$.

(D) Representative confocal micrographs of mitochondria in week 1 control and reprogramming cells stained with MitoTracker Deep Red and TMRE. White boxes indicate zoomed-in regions. Scale bar: 5 μm.

(E) Violin plots showing raw measurements of mitochondria for control mnCFs ($n = 360$) and putative iCMs ($n = 53$) at reprogramming week 1. Significance was determined by Kolmogorov-Smirnov test; *n* is cells. *$p < 0.05$, **$p < 0.01$, ***$p < 0.001$, and ****$p < 0.0001$.

(F) Violin plots showing SinCe^2 summary metrics higher in mnCFs. Data shown compare control mnCFs ($n = 360$) and putative iCMs ($n = 53$) at reprogramming week 1. Significance was determined by Kolmogorov-Smirnov test; *n* is cells. *$p < 0.05$, **$p < 0.01$, ***$p < 0.001$, and ****$p < 0.0001$.

(G) Violin plots showing SinCe^2 summary metrics higher in mnCMs. Data shown compare control mnCFs ($n = 360$) and putative iCMs ($n = 53$) at reprogramming week 1. Significance was determined by Kolmogorov-Smirnov test; *n* is cells. *$p < 0.05$, **$p < 0.01$, ***$p < 0.001$, and ****$p < 0.0001$.

(H) Reprogramming scores for control mnCFs ($n = 360$) and putative iCMs ($n = 53$) at reprogramming week 1, where *n* is cells.

(I) Representative confocal micrographs of mitochondria in week 4 control (CF) and reprogramming (iCM) cells stained with MitoTracker Deep Red and TMRE. White boxes indicate zoomed-in regions. Scale bar: 5 μm.

(J) Violin plots showing raw measurements of mitochondria for control mnCFs ($n = 44$) and putative iCMs ($n = 60$) at reprogramming week 4. Significance was determined by Kolmogorov-Smirnov test; *n* is cells. *$p < 0.05$, **$p < 0.01$, ***$p < 0.001$, and ****$p < 0.0001$.

(K) Violin plots showing SinCe^2 CF score metrics. Data shown compare control mnCFs ($n = 44$) and putative iCMs ($n = 60$) at reprogramming week 4. Significance was determined by Kolmogorov-Smirnov test; *n* is cells. *$p < 0.05$, **$p < 0.01$, ***$p < 0.001$, and ****$p < 0.0001$.

(L) Violin plots showing SinCe^2 summary CM score metrics. Data shown compare control mnCFs ($n = 44$) and putative iCMs ($n = 60$) at reprogramming week 4. Significance was determined by Kolmogorov-Smirnov test; *n* is cells. *$p < 0.05$, **$p < 0.01$, ***$p < 0.001$, and ****$p < 0.0001$.

(M) Reprogramming scores of control mnCFs ($n = 44$) and putative iCMs ($n = 60$) at reprogramming week 4, where *n* is cells.

(N) Representative TEM micrographs of CF controls (top) and iCMs (bottom) after week 6 of reprogramming, including 2 weeks of culture in media designed to induce spontaneous beating. Scale bars: 0.5 μm (left) and 1 μm (right) as denoted in images.

(O) Violin plots showing quantification of average mitochondrial area and cristae density in control and reprogramming cells. Each dot quantifies a discreet mitochondrial element, and data are pooled from TEM images of 5 cells from each culture. Significance was determined by Student's t test (CF $n = 122$, iCM $n = 120$); n is discreet mitochondrial elements. For statistical significance, $*p < 0.05$, $**p < 0.01$, $***p < 0.001$, and $****p < 0.0001$.
(P) Heatmap showing expression from RT-qPCR of mitochondrial genes and genes relevant to mitochondrial morphology in control (mnCF) and reprogramming (iCM) cultures at reprogramming week 2 ($n = 3$).
(Q) Cartoon depicting mitochondrial and metabolic reprogramming characteristics of cardiac reprogramming.

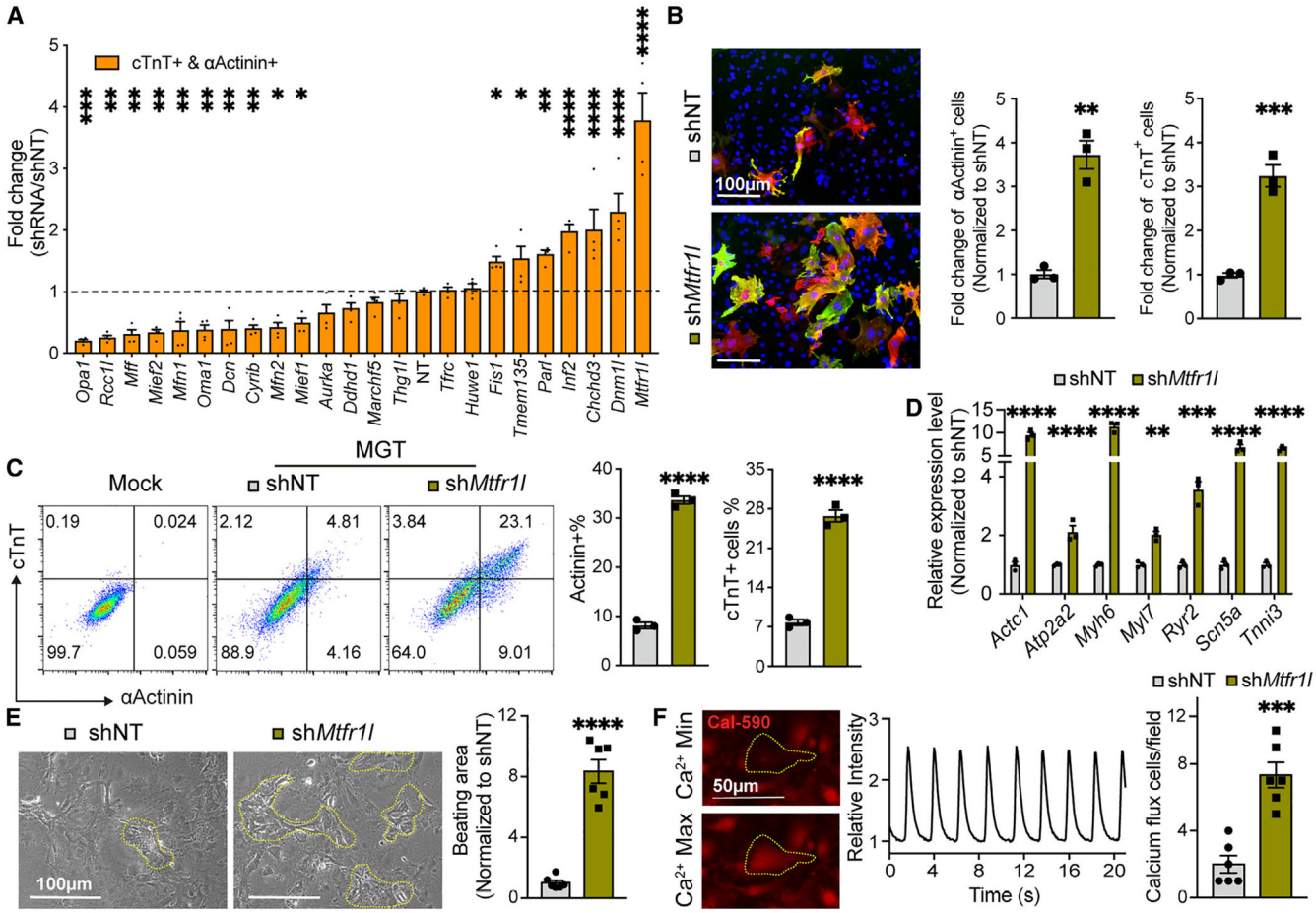

Figure 3. Silencing of a subset of fission regulators, particularly *Mtfr1l*, improves iCM conversion and maturation

(A) Bar graph quantifying the fold change of the percentage of cTnT+ α-Actinin+ cells in a loss-of-function screen for a panel of regulators and effectors of mitochondrial dynamics compared to a non-targeting control shRNA (shNT or NT). Significance was determined by one-way ANOVA followed by pairwise testing ($n = 4$). Data are presented as mean ± SEM; n is biological replicates. For statistical significance, *$p < 0.05$, **$p < 0.01$, ***$p < 0.001$, and ****$p < 0.0001$.

(B) Left: representative fluorescence micrographs of IF for cTnT and α-Actinin of reprogramming cultures with either sh*Mtfr1l* or shNT. Scale bar: 100 μm. Right: bar graphs quantifying proportion of α-Actinin+ and cTnT+ cells in replicate wells normalized to non-targeting control. Significance was determined using a Student's t test ($n = 3$). Data are presented as mean ± SEM; n is biological replicates. For statistical significance, *$p < 0.05$, **$p < 0.01$, ***$p < 0.001$, and ****$p < 0.0001$.

(C) Left: representative flow cytometry dot plots in pseudocolor comparing single- and double-positive cell populations for cTnT and α-Actinin in CF controls (mock), MGT+shNT, and MGT+sh*Mtfr1l*. Right: bar graphs quantifying proportion of α-Actinin+ and cTnT+ cells from flow cytometry normalized to non-targeting control. Significance was determined using a Student's t test ($n = 3$). Data are presented as mean ± SEM; n is

biological replicates. For statistical significance, *$p < 0.05$, **$p < 0.01$, ***$p < 0.001$, and ****$p < 0.0001$.

(D) RT-qPCR of CM markers between control (shNT) and sh*Mtfr1l* reprogramming cultures. Significance was determined using a Student's t test ($n = 3$). Data are presented as mean ± SEM; n is biological replicates. For statistical significance, *$p < 0.05$, **$p < 0.01$, ***$p < 0.001$, and ****$p < 0.0001$.

(E) Left: representative bright-field micrographs with spontaneously beating loci outlined in yellow. Scale bar: 100 μm. Right: bar graph quantifying spontaneously beating loci normalized to non-targeting control. Significance was determined using a Student's t test ($n = 6$). Data are presented as mean ± SEM; n is biological replicates. For statistical significance, *$p < 0.05$, **$p < 0.01$, ***$p < 0.001$, and ****$p < 0.0001$.

(F) Left: representative fluorescence micrographs showing the maximum and minimum fluorescence of a calcium-sensitive dye in an MGT+sh*Mtfr1l* cell exhibiting calcium transients. Scale bar: 50 μm. Middle: representative plot of calcium flux over time from the same cell. Right: bar graph quantifying proportion of cells exhibiting calcium transients normalized to non-targeting control. Significance was determined using a Student's t test ($n = 6$). Data are presented as mean ± SEM; n is biological replicates. For statistical significance, *$p < 0.05$, **$p < 0.01$, ***$p < 0.001$, and ****$p < 0.0001$.

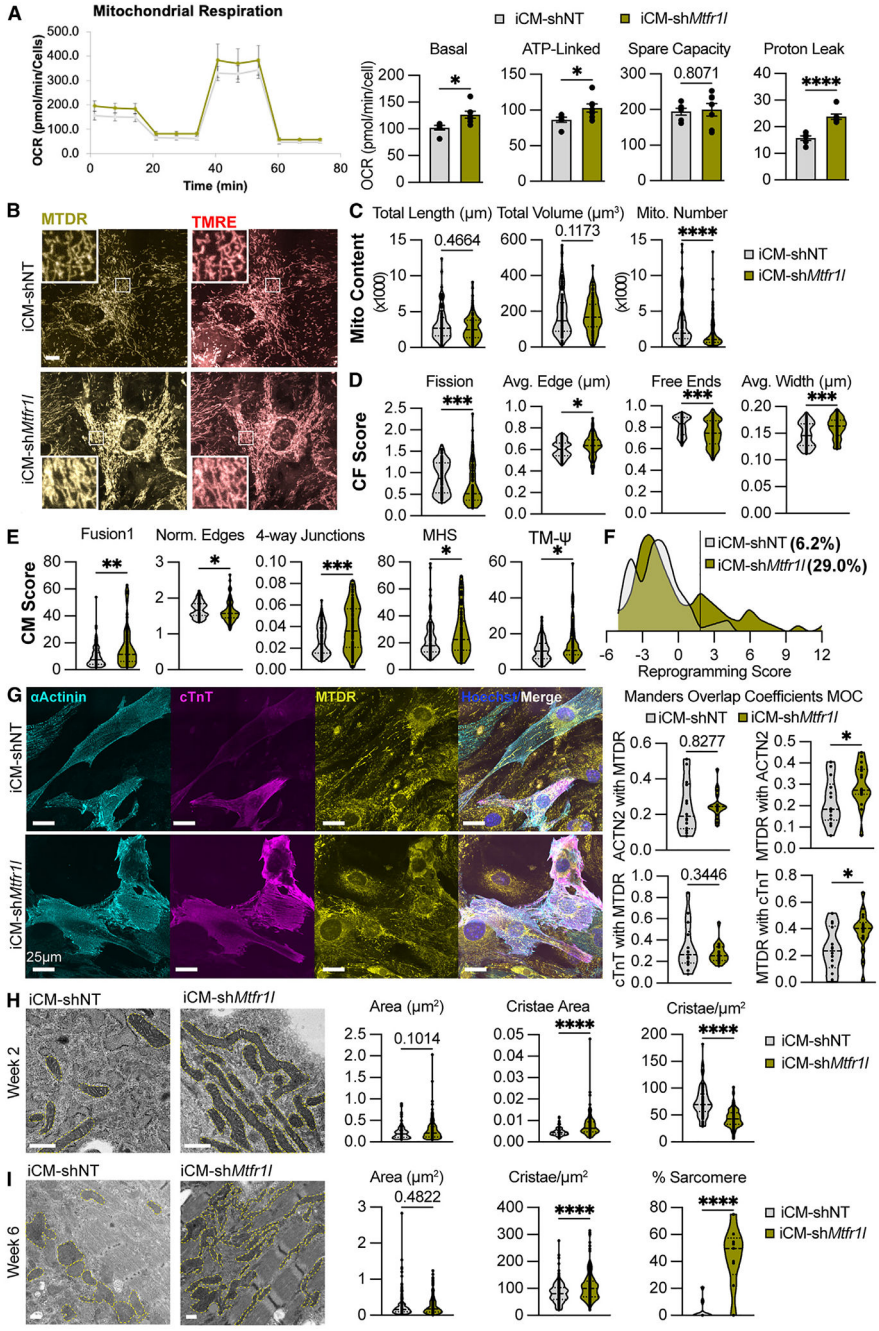

Figure 4. Loss of *Mtfr1l* alters the mitochondrial energetics and morphology of putative iCMs to more closely resemble those of native CMs

(A) Left: line graphs showing oxygen consumption rates (OCRs) over time of cardiac reprogramming cultures with sh*Mtfr1l* ($n = 7$) or shNT ($n = 6$) during a Seahorse mitochondrial stress test at reprogramming week 2. Data are presented as mean ± SD. Right: bar graphs showing quantification of biologically meaningful mitochondrial energetics. From left to right: OCR associated with generation of ATP, total basal mitochondrial OCR, mitochondrial OCR above the basal rate cells could use to respond to new stimuli, and the

OCR associated with ETS proton leak and ROS generation. Significance was determined by Student's t test. Data are presented as mean ± SEM; *n* is biological replicates.

(B) Representative confocal micrographs of mitochondria in reprogramming week 2 cells expressing shNT or sh*Mtfr1l* stained with MitoTracker Deep Red (MTDR) and TMRE. White boxes indicate zoomed-in regions. Scale bar: 5 μm.

(C) Violin plots showing raw measurements of mitochondria between shNT ($n = 112$) and sh*Mtfr1l* ($n = 93$) reprogrammed iCMs. Significance was determined by Kolmogorov-Smirnov test; *n* is cells. *$p < 0.05$, **$p < 0.01$, ***$p < 0.001$, and ****$p < 0.0001$.

(D) Violin plots showing SinCe^2 CF score metrics between shNT ($n = 112$) and sh*Mtfr1l* ($n = 93$) reprogrammed iCMs. Significance was determined by Kolmogorov-Smirnov test; *n* is cells. *$p < 0.05$, **$p < 0.01$, ***$p < 0.001$, and ****$p < 0.0001$.

(E) Violin plots showing SinCe^2 CM score metrics between shNT ($n = 112$) and sh*Mtfr1l* ($n = 93$) at 4 weeks of reprogramming. Significance was determined by Kolmogorov-Smirnov test; *n* is cells. *$p < 0.05$, **$p < 0.01$, ***$p < 0.001$, and ****$p < 0.0001$.

(F) Reprogramming score of shNT ($n = 112$) or sh*Mtfr1l* ($n = 93$) reprogrammed iCMs.

(G) Left: representative confocal micrographs of IF for sarcomeric (cTnT and α-Actinin) and mitochondrial markers (MTDR) as labeled in reprogramming week 2 cells expressing shNT ($n = 14$) or sh*Mtfr1l* ($n = 18$). Hoescht was used to stain nuclei. Scale bar: 5 μm. Right: violin plots showing quantification of correlation Manders overlap coefficients for sarcomeric cTnT and α-Actinin mitochondrial MTDR within whole-cell regions of interest (ROIs). Significance was determined by Student's t test; *n* is biological replicates. *$p < 0.05$, **$p < 0.01$, ***$p < 0.001$, and ****$p < 0.0001$.

(H) Left: representative TEM micrographs of putative iCMs expressing shNT or sh*Mtfr1l* after week 2 of reprogramming. Scale bars: 0.5 μm. Right: violin plots of average mitochondrial area, average cristae area, and cristae density in control ($n = 90$) and knockdown ($n = 134$) cells. Each dot quantifies a discreet mitochondrial element, and data are pooled from TEM images of 5 cells from each culture. Significance was determined by Student's t test; *n* is discreet mitochondrial elements or cells as noted. *$p < 0.05$, **$p < 0.01$, ***$p < 0.001$, and ****$p < 0.0001$.

(I) Left: representative TEM micrographs of putative iCMs expressing shNT or sh*Mtfr1l* after week 6 of reprogramming, including 2 weeks of culture in media designed to induce spontaneous beating. Scale bars: 0.5 μm. Right: violin plots showing quantification of average mitochondrial area (shNT $n = 236$, sh*Mtfr1l* $n = 209$), cristae density, and formed sarcomeric structures ($n = 9$) in control and knockdown cells. Each dot quantifies a discreet mitochondrial element, and data are pooled from TEM images of 9 cells from each culture. Significance was determined by Student's t test; *n* is discreet mitochondrial elements or cells as noted. For statistical significance, *$p < 0.05$, **$p < 0.01$, ***$p < 0.001$, and ****$p < 0.0001$.

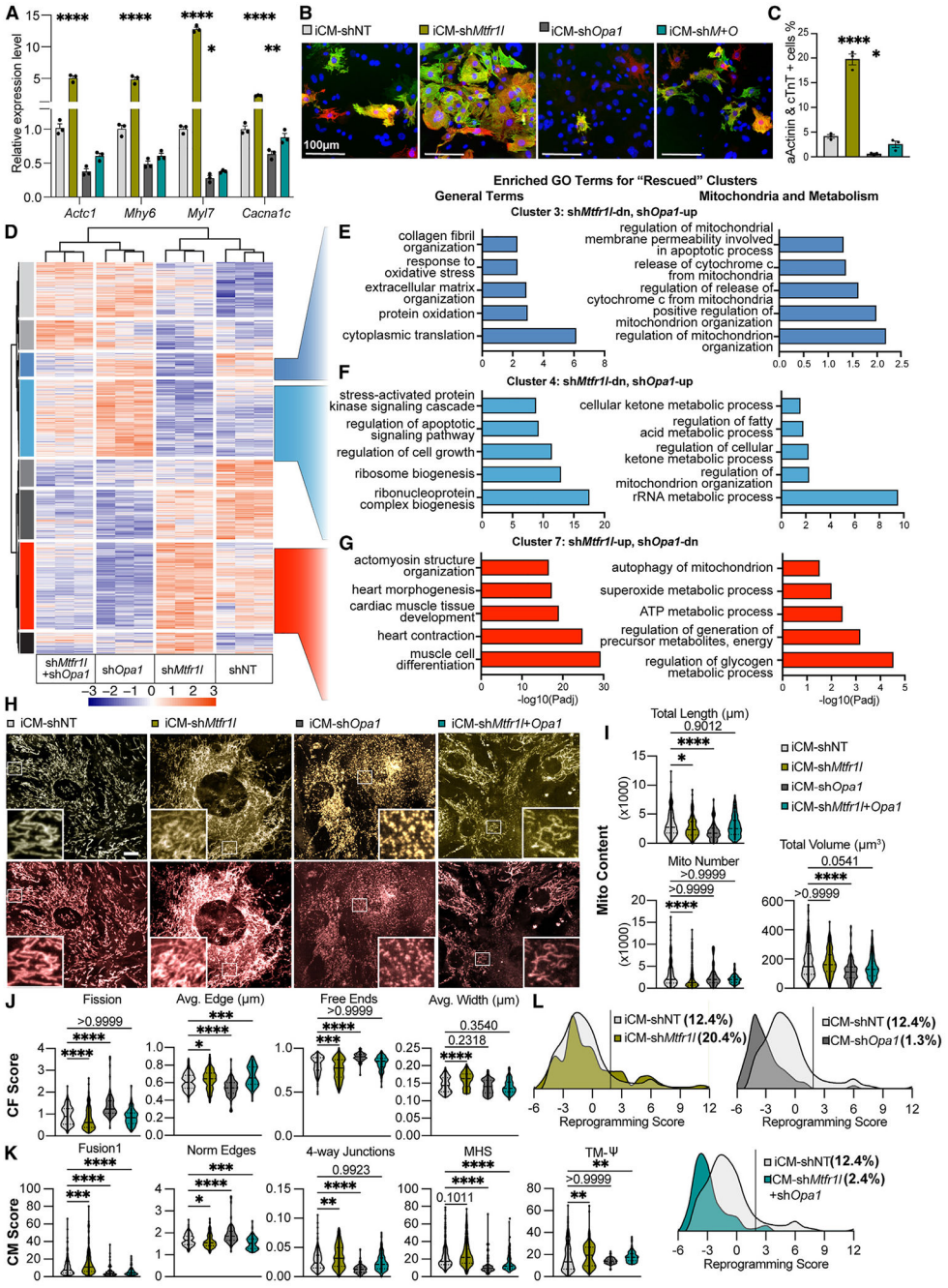

Figure 5. Loss of *Mtfr1l* primes CFs for cell fate conversion to iCMs in an Opa1-dependent mechanism

(A) RT-qPCR of CM genes between reprogramming groups: iCM-shNT (light gray), iCM-sh*Mtfr1l* (olive green), iCM-sh*Opa1* (dark gray), and iCM-sh*Mtfr1l*+*Opa1* (dark teal). Data are presented as mean ± SEM. Significance was determined using one-way ANOVA followed by pairwise testing ($n = 3$); n is biological replicates. For statistical significance, *$p < 0.05$, **$p < 0.01$, ***$p < 0.001$, and ****$p < 0.0001$.

(B) Representative IF images for sarcomere markers (cTnT and α-Actinin) between reprogramming groups expressing shNT, sh*Mtfr1l*, sh*Opa1*, or both. Scale bar: 100 μm.

(C) Quantification of cells in replicate wells double positive for sarcomere markers cTnT and α-Actinin. Data are presented as mean ± SEM. Significance was determined using one-way ANOVA followed by pairwise testing ($n = 3$); n is biological replicates. For statistical significance, *$p < 0.05$, **$p < 0.01$, ***$p < 0.001$, and ****$p < 0.0001$.
(D) Heatmap of differentially expressed genes (DEGs) in bulk RNA-seq data.
(E) Bar graph of significance of enriched GO terms identified in cluster 3 from hierarchical clustering showing downregulation in sh*Mtfr1l* and upregulation in sh*Opa1* compared to shNT up in putative iCMs. General GO terms are shown on the left, and mitochondrial and metabolic-specific terms are shown on the right.
(F) Bar graph of significance of enriched GO terms identified in cluster 4 from hierarchical clustering showing downregulation in sh*Mtfr1l* and upregulation in sh*Opa1* compared to shNT down in putative iCMs. General GO terms are shown on the left, and mitochondrial and metabolic-specific terms are shown on the right.
(G) Bar graph of significance of enriched GO terms identified in cluster 7 from hierarchical clustering showing upregulation in sh*Mtfr1l* and downregulation in sh*Opa1* putative iCMs. General GO terms are shown on the left, and mitochondrial and metabolic-specific terms are shown on the right.
(H) Representative fluorescence micrographs of IF for cTnT and α-Actinin of reprogramming cultures with sh*Mtfr1l*, sh*Opa1*, a combination of both or shNT. White boxes represent zoomed-in regions. Scale bar: 5 μm.
(I) Violin plots showing raw measurements of mitochondria between sh*Mtfr1l* ($n = 186$), sh*Opa1* ($n = 76$), a combination of both ($n = 83$), and shNT ($n = 194$) reprogrammed iCMs. Significance was determined using Kruskal-Wallis followed by pairwise testing; n is cells. For statistical significance, *$p < 0.05$, **$p < 0.01$, ***$p < 0.001$, and ****$p < 0.0001$.
(J) Violin plots showing $SinCe^2$ summary metrics found to be higher in mnCFs between sh*Mtfr1l* ($n = 186$), sh*Opa1* ($n = 76$), a combination of both ($n = 83$), and shNT ($n = 194$) reprogrammed iCMs. Color coding is described in (I). Significance was determined using Kruskal-Wallis followed by pairwise testing; n is cells. For statistical significance, *$p < 0.05$, **$p < 0.01$, ***$p < 0.001$, and ****$p < 0.0001$.
(K) Violin plots showing $SinCe^2$ summary metrics higher in mnCMs between sh*Mtfr1l* ($n = 186$), sh*Opa1* ($n = 76$), a combination of both ($n = 83$), and shNT ($n = 194$) reprogrammed iCMs. Color coding is described in (I). Significance was determined using Kruskal-Wallis followed by pairwise testing; n is cells. For statistical significance, *$p < 0.05$, **$p < 0.01$, ***$p < 0.001$, and ****$p < 0.0001$.
(L) Reprogramming scores of sh*Mtfr1l* ($n = 186$), sh*Opa1* ($n = 76$), and a combination of both ($n = 83$) with shNT ($n = 194$) reprogrammed iCMs, where n is cells.

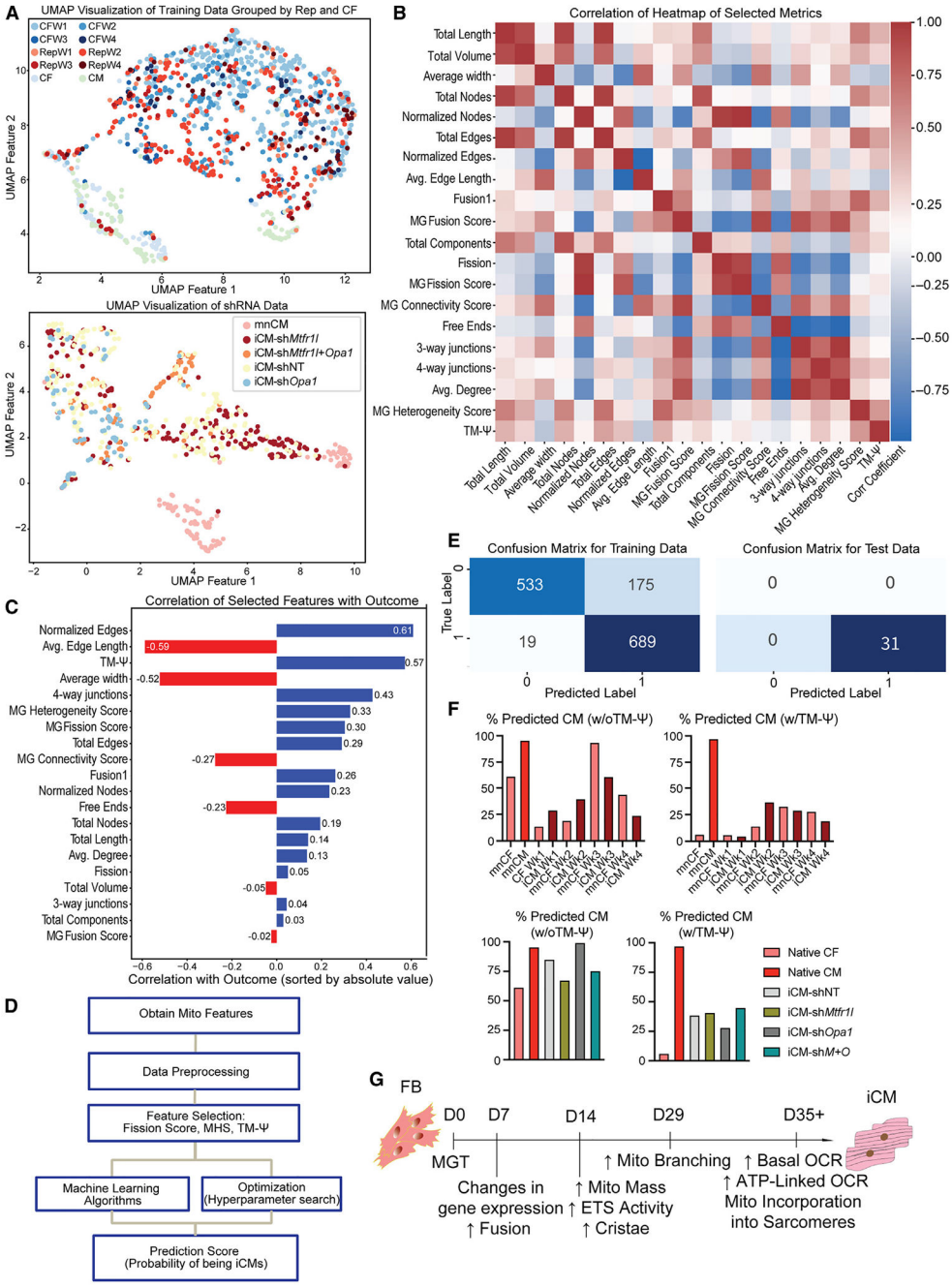

Figure 6. Using machine learning to predict reprogramming in live cells at early time points using only mitochondrial phenotypes

(A) UMAP plots showing clustering of reprogramming cultures and controls for reprogramming time points (top) and shRNAs (bottom) compared to native CFs and CMs.

(B) Correlation heatmap showing relationships between various MitoSinCe[2] metrics.

(C) Bar graph showing the correlation of each metric with the outcome of CM in our model.

(D) Schematic showing the strategy for building a machine learning model for predicting reprogramming based on mitochondrial phenotypes.

(E) Tables showing the capacity of the model to classify both the training dataset and a test dataset of iCMs expressing sarcomeric markers.
(F) Bar graphs showing the proportion of cells the model predicts to be CMs based on mitochondrial metrics for the reprogramming time course (top) and the shRNAs (bottom). Two versions of the model are presented: one excluding TMRE (left) and one including TMRE (right).
(G) Timeline of observed mitochondrial changes during cardiac reprogramming.

KEY RESOURCES TABLE

REAGENT or RESOURCE	SOURCE	IDENTIFIER
Antibodies		
Alexa Fluor 488 AffiniPure Donkey Anti-Mouse IgG (H + L)	Jackson Immunoresearch	Cat# 715-545-150; RRID: AB_2340846
Alexa Fluor 647 AffiniPure Donkey Anti-Rabbit IgG (H + L)	Jackson Immunoresearch	Cat# 715-605-152; RRID:AB_2492288
Anti-Sarcomeric Alpha Actinin antibody	Abcam	Cat# ab68167; RRID:AB_11157538
Beta Actin Antibody (C4)	Santa Cruz	Cat# sc-47778; RRID:AB_626632
Cardiac Troponin T Monoclonal Antibody (13-11)	Invitrogen	Cat# MA5-12960; RRID:AB_11000742
Donkey anti-Mouse HRP	Jackson Immunoresearch	Cat# 715-035-150; RRID:AB_2340770
Donkey anti-Rabbit HRP	Jackson Immunoresearch	Cat# 711-035-152; RRID:AB_10015282
DRP1 (D8H5) Rabbit Monoclonal Antibody	Cell Signaling Technology	Cat# 5391S; RRID:AB_10557420
HSP60 (D6F1) XP Rabbit Monoclonal Antibody	Cell Signaling Technology	Cat# 12165; RRID:AB_2636980
CD90.2 (Thy-1.2) Monoclonal Antibody (53–2.1)	Thermo Fisher Scientific	Cat# 13-0902-85, RRID:AB_466534
OPA1 (D6U6N) Rabbit Monoclonal Antibody	Cell Signaling Technology	Cat# 80471S; RRID:AB_2734117
MTFR1L Polyclonal Antibody	Invitrogen	Cat# PA5-55516; RRID:AB_2644256
Chemicals, peptides, and recombinant proteins		
4%–20% acrylamide gel	Biorad	Cat# 4561096
ACK Lysis Buffer	ThermoFisher	Cat # A1049201
Acutase	StemCellTechnologies	Cat# 07920
Antimycin A	Sigma	Cat# A8674
L-Ascorbic acid	Sigma	Cat# A92902
Bovine Serum Albumin (BSA)	Sigma	Cat# A3294
cOmplete EDTA-free Protease Inhibitor cocktail	Roche	Cat# 5892791001
Dulbecco's Phosphate Buffered Saline (DPBS)	Corning	Cat# 21-031-CV
Dulbecco's Modified Eagle Medium (DMEM)	Corning	Cat# 10-013-CV
Carbonyl Cyanide *m*-Chlorophenylhydrazone (CCCP)	Sigma	Cat# C2759
Collagenase II	Worthington	Cat# LS004177
Collagenase IV	Worthington	Cat# LS0004189
Glutaraldehyde	Sigma	Cat# 80424-50MG-F
Fetal Bovine Serum (FBS)	Sigma	Cat# F2442
Hanks Balanced Salt Solution (HBSS	Corning	Cat# 21-022-CV
Hoechst 33342, trihydrochloride trihydrate	ThermoFisher	Cat# H1399
Iscove's Modified Dulbecco's Medium (IMDM)	Gibco	Cat# 12440053
Lamelli Loading Buffer (2X)	BioRad	Cat# 1610737
Lipofectamine 2000	ThermoFisher	Cat# 11668019

REAGENT or RESOURCE	SOURCE	IDENTIFIER
Media 199	Coring	Cat# 10-060-CV
MitoTracker Deep Red FM	Invitrogen	Cat# M22426
Nuclease-Free Water (not DEPC-Treated	Invitrogen	Cat# AM9937
Oligomycin	Sigma	Cat# O4876
Penicillin-Streptomycin	Gibco	Cat# 15070063
PEG-4000	Sigma	Cat# 81260-5KG
Paraformaldehyde 32% Aqueous Solution EM Grade	Electron Microscopy Sciences	Cat# 15714-S
Polybed 812 epoxy resin	Polysciences, Inc.	Cat# 08791-500
Polybrene	EMD Millipore	Cat# TR-1003-G
PhosStop Phosphatase Inhibitor Cocktail Tablets	Roche	Cat# 4906845001
RIPA Buffer	Thermofisher	Cat# 89900
Recombinant Human FGF basic/FGF2/bFGF (146 aa) Protein	R&D Systems	Cat# 233-FB-025/CF
Recombinant Human FGF-10 Protein	R&D Systems	Cat# 345-FG-025/CF
Recombinant Human VEGF 165 Protein R&D Systems 293-VE-010/CF	R&D Systems	Cat# 293-VE-010/CF
Reynold's lead citrate	Reynold's	Cat# 1963
Rotenone	Sigma	Cat# R8875
Sodium Phosphate	Sigma	Cat# S8282
Stempro-34 SF medium	ThermoFisher	Cat# 10639011
Super Script IV Master Mix	Invitrogen	Cat# 11756-500
SuperSignal West Pico PLUS Chemiluminescent Substrate	ThermoFisher	Cat# 34579
SYBR Green PCR Master Mix	Fisher	Cat# 43-1127-04
Tetramethylrhodamine Ethyl Ester Perchlorate (TMRE)	Sigma	Cat# 87917
Tris-Buffered Saline (10X)	Boston BioProducts	Cat# BM-301
TRIzol RNA Isolation Reagent	Invitrogen	Cat# 15596026
Triton X-100	Fisher	Cat# BP151-100
0.05% Trypsin-EDTA	Gibco	Cat# 253000-054
Tween 20	Sigma	Cat# P6585
Uranyl Acetate	Electron Microscopy Sciences	Cat# 22400-4
Critical commercial assays		
BD Cytofix/Cytoperm™ Fixation/ Permeabilization Kit	BD Bioscience	Cat# 554714
Calbryte 590 a.m.	AAT Bioquest	Cat# 20700
Live cell Microcopy chambers (μ-Slide 8 Well high Grid-50)	IBIDI	Cat# 80806-96
Lowry Assay	Biorad	Cat# 5000111
Neonatal Cardiomyocyte isolation System	Worthington Biochemical Corporation	Cat# LK003300

REAGENT or RESOURCE	SOURCE	IDENTIFIER
Seahorse Cell Culture Plates	Agilent	Cat# 101085
Deposited data		
RNAseq	GEO Repository	GEO: GSE269231
Experimental models: Cell lines		
HEK 293T	ATCC	CRL-3216
PlatE	Cell Biolabs	RV-101
Cardiac fibroblast	Isolated from neonatal pups and adult mice age 3–4 months	
Mouse Embryonic fibroblast	Isolated from E13,5 mouse embryo	
Cardiomyocyte	Isolated from neonatal pups	
Experimental models: Organisms/strains		
CD-1	Charles River	022
Oligonucleotides		
qRT-PCR primers	This manuscript	Table S1
Recombinant DNA		
pMD2.G		Addgene_12259
pMx-puro-MGT	Garbutt et al.[59]	Addgene_111809
psPAX2	gift from Didier Trono	Addgene_12260
shRNA	Sigma	Table S2
Software and algorithms		
BiOP plug-in in FIJI		
BBMap	Bushnell et al.[60]	https://sourceforge.net/projects/bbmap/
clusterProfiler	Wu et al.[61]	https://bioconductor.org/packages/release/bioc/html/DESeq2.html
DESeq2	Love et al.[62]	https://bioconductor.org/packages/release/bioc/html/DESeq2.html
FastQC	Babraham Bioinformatics	https://ww.bioinformatics.babraham.ac.uk/projects/fastqc/
FlowJo 10.10.0	FlowJo LLC	https://www.flowjo.com/
GraphPad Prism version 10	GraphPad Software	https://www.graphpad.com/scientificsoftware/prism/
Gatan Microscopy Suite 3.0	Gatan Inc.	https://www.gatan.com/products/tem-analysis/gatan-microscopy-suite-software
GSEABase	Martin Morgan[63]	https://www.bioconductor.org/packages/release/bioc/html/GSEABase.html
ImageJ-FIJI	National Institutes of Health, USA	https://fiji.sc/
Imblearn 0.12.4	Lemaître et al.[64]	https://imbalanced-learn.org/stable/
Matplotlib 3.9.2	Hunter et al.[65]	https://matplotlib.org/stable/
MitoGraph v3.0	Viana et al.[44]	https://github.com/vianamp/MitoGraph
NumPy 2.1.0	Oliphant[66]	https://numpy.org/doc/2.1/index.html
Pandas 2.2.3	McKinney[67]	https://pandas.pydata.org/
R version 4.3.0		https://www.r-project.org
scikit-learn 1.5.1	Pedregosa et al.[68]	https://scikit-learn.org/stable/

REAGENT or RESOURCE	SOURCE	IDENTIFIER
Xgboost 2.1.1	Chen and Guestrin[69]	https://xgboost.readthedocs.io/en/stable/